THESIS APPROVAL

GRADUATE SCHOOL, KASETSART UNIVERSITY

Master of Science (Chemistry)
DEGREE

Chemistry
FIELD

Chemistry
DEPARTMENT

TITLE: Structures and Electronic Properties of Oligo(*p*-phenylenevinylene) Carboxylic Acid and Its Derivatives: Effects of Spacer and Anchor Groups by Theoretical Methods

NAME: Mr. Apipol Piriyagagoon

THIS THESIS HAS BEEN ACCEPTED BY

THESIS ADVISOR
(Associate Professor Supa Hannongbua, Dr.rer.nat.)

THESIS CO-ADVISOR
(Mr. Chak Sangma, Ph.D.)

THESIS CO-ADVISOR
(Assistant Professor Wirunya Keawwattana, Ph.D.)

THESIS CO-ADVISOR
(Mr. Songwut Suramitr, Ph.D.)

DEPARTMENT HEAD
(Assistant Professor Noojaree Prasitpan, Ph.D.)

APPROVED BY THE GRADUATE SCHOOL ON

DEAN
(Associate Professor Gunjana Theeragool, D.Agr.)

THESIS

STRUCTURES AND ELECTRONIC PROPERTIES OF OLIGO(*P*-PHENYLENEVINYLENE) CARBOXYLIC ACID AND ITS DERIVATIVES: EFFECTS OF SPACER AND ANCHOR GROUPS BY THEORETICAL METHODS

APIPOL PIRIYAGAGOON

A Thesis Submitted in Partial Fulfillment of
the Requirements for the Degree of
Master of Science (Chemistry)
Graduate School, Kasetsart University
2009

Apipol Piriyagagoon 2009: Structures and Electronic Properties of Oligo(*p*-phenylenevinylene) Carboxylic Acid and Its Derivatives: Effects of Spacer and Anchor Groups by Theoretical Methods. Master of Science (Chemistry), Major Field: Chemistry, Department of Chemistry. Thesis Advisor: Associate Professor Supa Hannongbua, Dr.rer.nat. 95 pages.

A series of DPO-OPV3-COOH organic chromophore was investigated as sensitizers for DSSCs. The structures and electronic properties were studied by quantum chemical calculations. All structures were optimized using HF/6-31G* and B3LYP/6-31G* methods. The vertical excitation energies were calculated using TD-B3LYP/6-31G* method based on ground state geometry optimization. The structure obtained from HF/6-31G* method is found that coplanar conformation. Conversely, that of B3LYP/6-31G* method showed planar conformation. In addition, the electronic transitions were calculated to confirm the most reliable configuration structure from different methods. The simulated absorption spectrum of HF/6-31G* coplanar optimized structure is in well agreement with experimental absorption data than that of B3LYP/6-31G* planar optimized structure. Therefore, in this study, TD-B3LYP/6-31G*//HF/6-31G* and coplanar conformation were selected to further study on the effects of spacer and anchor groups.

For DPO-OPV3-COOH derivatives, phenylenevinylene and carboxylic acid take the role of electron donor and electron acceptor, respectively. The introduction of various thiophene spacer groups to form donor-spacer-acceptor configuration lead to superior performance over the simple donor-acceptor configuration, in terms of bathochromically extended absorption spectra and enhances the electron transfer in the molecule. Moreover, the present study of the modeling in terms of methoxy side chain, di-vinylene-thiophene spacer, and acrylic acid anchor group, the new sensitizer of DMO-OPV3-di-Vi-Th-CN-COOH is therefore suggested for the further study and synthesis.

____________________ ____________________ ___ / ___ / ___

Student’s signature Thesis Advisor’s signature

ACKNOWLEDGEMENTS

I sincerely thank my advisor, Associate Professor Dr. Supa Hannongbua for her tremendous support and meticulous attention throughout the duration of my graduate study and research. I also wish to express my appreciation to my advisory committee Assistant Professor Dr. Wirunya Keawwattana, Dr. Chak Sangma and Dr. Songwut Suramitr, the representative of Graduate School, for their worthy suggestion and constructive criticism.

I would like to express my deep gratitude to The Development and Promotion of science and Technology Talents project (DPST), Commision on Higher Education (CHE), and The Postgraduate Education and Research Program in Petroleum, Petrochemical Technology and Advance Materials for financial supports. My colleagues at Laboratory for Computational and Applied Chemistry (LCAC) are sincere thanked for their providing helpful assistance and sharing useful ideas and I would also like to thank all of staffs at Department of Chemistry, Faculty of Science, Kasetsart University for research facilities.

Finally, I wish to thanks my family and friends for their advice, encouragement and understanding.

Apipol Piriyagagoon
March, 2009

TABLE OF CONTENTS

LIST OF TABLES

LIST OF TABLES (Continued)

LIST OF FIGURES

LIST OF FIGURES (Continued)

Figure **Page**

LIST OF FIGURES (Continued)

Figure **Page**

LIST OF FIGURES (Continued)

LIST OF ABBREVIATIONS

AM1 = Austin Model 1

AOs = Atomic Orbitals

B3LYP = Becke's three parameter hybrid functional using the LYP correlation functional

DFT = Density Functional Theory

CIS = Configuration Interaction Singles

DPO-PPV = Oligo(2,5-penthoxy-PPV)

DMO-PPV = Oligo(2,5-methoxy-PPV)

DHO-PPV = Oligo(2,5-hexyloxy-PPV)

FT-IR = Fourier Transform Infra-Red spectroscopy

GTO = Gaussian-Type Orbital

HF = Hartree-Fock

^{1}H-NMR = Proton Nuclear Magnetic Resonance

HOMO = Highest Occupied Molecular Orbital

KS = Kohn-Sham

LCAO = Linear Combination of Atomic Orbitals

LCAO-MO = Linear Combination of Atomic Orbitals to Molecular Orbitals

LDA = Local Density Approximation

LSD = Local Spin Density Approximation

LUMO = Lowest Unoccupied Molecular Orbital

LYP = Lee-Yang-Parr functional

MNDO = Modified Neglect of Diatomic Overlap

MO = Molecular Orbital

MP2 = The second-order Møller-Plesset perturbation theory

PM3 = MNDO Parametric Method number 3

PPV = Poly(1,4-phenylene vinylene)

SCF = Self-Consistent Field

STRUCTURES AND ELECTRONIC PROPERTIES OF OLIGO(*p*-PHENYLENEVINYLENE) CARBOXYLIC ACID AND ITS DERIVATIVES: EFFECTS OF SPACER AND ANCHOR GROUPS BY THEORETICAL METHODS

INTRODUCTION

Today the world's nonrenewable supply of fossil fuel, which is oil, coal and natural gas, is depleted slowly because of continuous demand. The combustible emissions from vehicles, factories and other facilities undesirable affect the atmosphere, known as greenhouse gases. They do not only destroy the environment but also damage human health. Therefore, the renewable sources of energy are major interest. These alternative energies can be produced by the sun, wind, water or even garbage, plant remains and livestock manure. The latter source of electricity and fuels are so-called biomass. Thailand spent many billions baht to import oil. If self-renewing resources are of major intent to the country, it could lead to one of the solutions for our energy needs.

The Photovoltaic (PV) cell, commonly known as a solar cell, is a device that converts solar energy into electricity by the photovoltaic effect. Photovoltaic (literally meaning light-electricity) is the field of technology and research related to the application of solar cells as solar energy. Sometimes the term solar cell is reserved for devices intended specifically to capture energy from sunlight, while the term photovoltaic cell is used when the source is unspecified.

However, there are drawbacks of the renewable energy development. For example, solar thermal energy involving the collection of solar rays needs large tract of land, for the buildings, roads, transmission lines and transformers which disturbs the natural habitat of plants and animals. Additionally, solar or PV cells shares the same technologies with the production of silicon chips for computers whose manufacture requires toxic compounds used in batteries to store the power.

Even if PV cell is improved to be the green technology, another big problem must be overcome. However, the cost of producing solar electricity would be about four times more expensive than that of a regular natural gas-fired power plant. Even though the renewable power plant does not release air pollution or use precious fossil fuels, it still has an impact on the environment.

In a traditional solid-state semiconductor, a solar cell is made from two doped crystals, one with a slight negative bias (n-type semiconductor), which has extra free electron, and the other with a slight positive bias (p-type semiconductor), which lacks of free electrons. When placed in contact, some electrons in the n-type portion will flow into the p-type to fill in the missing electrons, known as an electron hole. Eventually, the Fermi levels of the two materials are equalized. The result is a region at the interface, thep-n junction, where charge carriers are depleted and accumulated on each side of the interface (Figure 1).

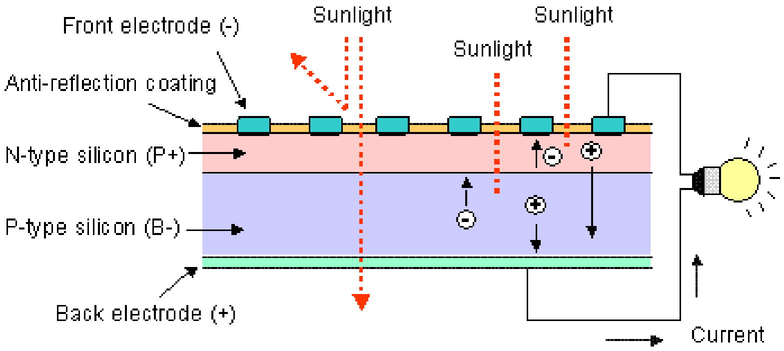

Figure 1 Mechanism of p-n junction solar cell

From the band theory of materials, the difference in energy between the valence and conduction bands, the bandgaps, means that only photons with that amount of energy, or more, will contribute to producing a current. Unfortunately this also means that the higher energy photons, at the blue and violet end of the spectrum, have more than enough energy to cross the bandgap, and although some of this energy is transferred into the electrons, much of it is wasted as heat. Another issue is the reasonable thickness of the cell required for capturing a photon in the p-type layer. This also increases the chance that a freshly-ejected electron will meet up with a hole in the material before reaching the p-n junction. These effects produce an upper limit on the efficiency of silicon solar cells, currently around 12-15% for common samples and up to 42.8% for the best laboratory modules.

Although these solar cells have high efficiency, by far the biggest problem with this conventional approach is the cost. It requires a relatively thick layer of silicon for the reasonable photon capture rates. This conventional component is an expensive commodity and toxic. Therefore, dye sensitization for photoelectric power generation was invented by Gratzel *et al*. (1991). The benefits of the novel solar cells are its simple fabrication, low cost and being environmentally friendly.

The dye-sensitized solar cell (DSSCs) is a relatively new class of thin film solar cell. It is based on a semiconductor formed between a photo-sensitized anode and an electrolyte, a photoelectrochemical system. This cell is promising because it costs less and does not need elaborate manufacturing apparatus. In bulk materials, it should be significantly less expensive than the solid-state cell designs. It can be engineered to be flexible sheets with mechanically robust, requiring no protection from minor events like hail or tree strikes. Although its conversion efficiency is less than the thin-film, its price/perfoemance ratio is high enough to compete with fossil fuel electrochemical generation.

The DSSCs separate two functions of silicon in a traditional cell design. Normally, silicon acts as both the source of photoelectrons, as well as providing the electric field that separates the charges and then create a current. In the DSSC, the bulk semiconductor is used solely for charge transport while the photoelectrons are provided from a separate photosensitive dye. Charge separation occurs at the surfaces between the dye, semiconductor and electrolyte. The solar cell consists of conductive electrode coat with nanocrystalline semiconductor (e.g. anatase TiO_2) that was adsorbed on a sensitizer, an liquid electrolyte bearing a redox couple (e.g. I_3^-/I^-) and counter electrode coat with regeneration of electrolyte (e.g. Pt) as shown in Figure 2.

Since dye molecules are quite small (nanometer sized), the layer of the molecules must be fairly thick, much thicker than the molecule size, to capture a reasonable amount of the incoming light. To address this problem, a nanomaterial is used as a scaffold to hold large numbers of molecules, increasing the number for any given surface area of the cell. In the nowadays designs, this scaffolding is provided in the semiconductor material.

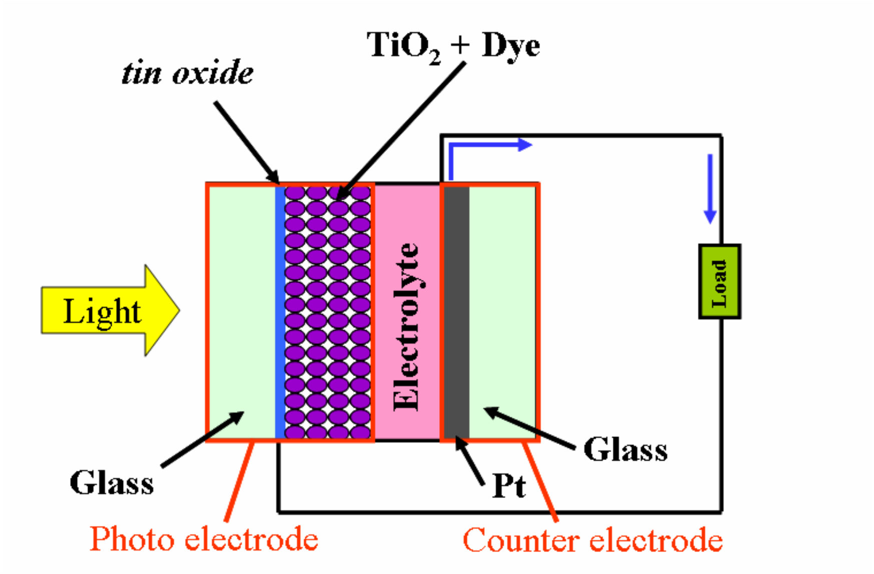

Figure 2 Components of dye sensitized solar cell

In the mechanism of DSSCs, light absorption is performed by a monolayer dye (sensitizer) adsorbed chemically on the semiconductor surface at the conductive electrode. Electrons of dye at ground state that adsorbs energy from light are excited. Electrons will be transferred from the excited state to the conduction band of semiconductor, reach conductive electrode via electrical circuit. Finally, it produces electricity and move toward the counter electrode. The electrolyte oxidized electrons at counter electrode then become reductive one. Afterward, it reduces electrons of dye for ground state and returns to the oxidation state. The dye sensitized solar cell is then prepared for a new light absorption (Figure 3 and Figure 4).

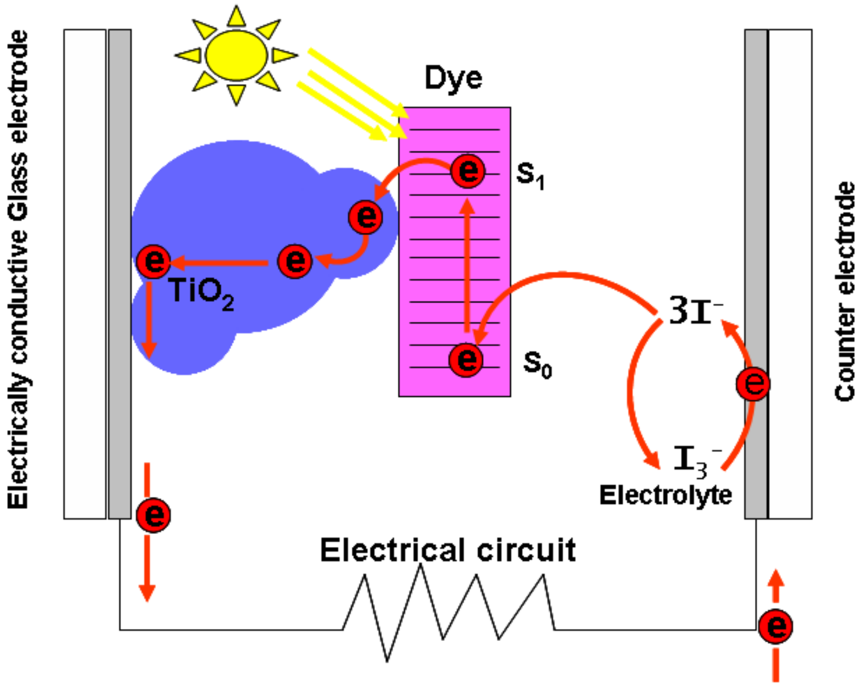

Figure 3 Mechanism of dye sensitized solar cell

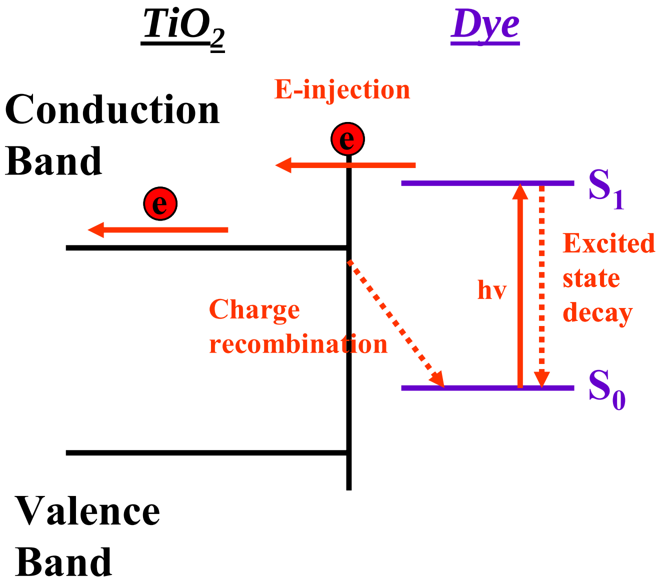

Figure 4 Electron transfer of dye sensitized solar cell

Reactions of electron transfer of dye sensitized solar cell are summarized below

The Anode electrode reactions

$TiO_2/S + h\nu \rightarrow TiO_2/S^*$ ------ (1)

$TiO_2/S^* \rightarrow TiO_2/S^+ + e_{cb}$ ------ (2)

$TiO_2/S^+ + e_{cb} \rightarrow TiO_2$ ------ (3)

The Cathode electrode reactions

$TiO_2/S^+ + 3/2\ I^- \rightarrow TiO_2/S + 1/2\ I_3^-$ ------ (4)

$1/2\ I_3^- + e_{(Pt)} \rightarrow 3/2\ I^-$ ------ (5)

$I_3^- + 2e_{cb} \rightarrow 3\ I^-$ ------ (6)

From these reactions, the efficiency of DSSCs can be increased by improving the light absorption of sensitizer, dye adsorption on semiconductor surface, the electron injection of an electron from a photoexcited state of the sensitizer dye into conduction band and the regeneration and degradation of liquid electrolyte. However, most researches take an interest to improve the first one.

The DSSCs using a metal dye of *cis*-di(thiocyanato)-bis(2,2’-bipyridyl-4,4’ dicarboxylate)ruthenium(II), henceforth refer to N3 (Figure 5), as the sensitizer was reported to have a conversion efficiency up to ~11% which is comparable to amorphous silicon-based PV cells and of practical utility (Nazeerudin *et al.*,2001).

After that, Wu *et al*. (2006) reported on the (bipyridine)Ru(II)-based dye exhibiting a relatively higher efficiency than N3 (8.54% vs 7.70%). Nevertheless, N3, N719 (*cis*-bis(isothiocyanato)bis(2,2’-bipyridyl-4,4’-dicarboxylato)-ruthidium(II)bis tetrabutylammonium) (Figure 6) and their congeners are still outstanding as the most reliable metal complex sensitizer with the efficiencies more than 7%

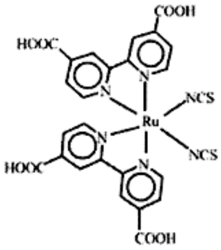

Figure 5 Molecular structure of N3 metal complex dye sensitizer

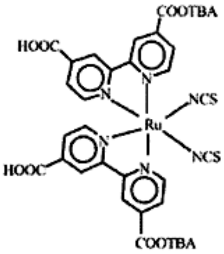

Figure 6 Molecular structures of N719 metal complex dye sensitizer

Metal complex sensitizers have attracted much attention due to their higher molar extinction coefficients and lower cost. Representative metal-free organic dyes include coumarin-, indolin- and perylene-based dyes. A few reports on thiophene based spacer exhibiting good device efficiencies make it become more interesting. Its impressive efficiency can be achieved for DSSCs based on the dyes even they have significantly shorter absorption wavelengths than the N3 dye. Apparently, high molar extinction coefficients, several other factors, such as minimization of charge recombination, broader spectral coverage and hydrophobicity are important in optimizing the sensitizer's new designs for the DSSCs.

Although the metal dye sensitizers in DSSCs have high extinction coefficients and efficiency, it pollutes the environments. Therefore, several research groups have synthesized organic, oligomers and dipolar dyes as a new alternative sensitizer. In general, such compounds possess both π-π* and charge-transfer absorption bands in the electronic spectra which correlate to the electron injection efficiency in DSSCs.

Most organic sensitizers constitute of donor, linker and acceptor. Generally, those used for the solar cells are expected to possess broad and intense spectral absorption in the visible light region, which is about 90% of wavelengths consisting in the sunlight. One strategy toward this end is to introduce more π-conjugation between the donor and acceptor. However, one segment already exists, which may facilitate the electron transfer. Good acceptors, like carboxylic group, bind with TiO_2 strongly.

The organic chromophores for DSSCs have drawn attention of many research groups. They reached efficiencies of 5-8%, for example 1*H*-phenanthro[9,10 *d*]imidazole, triarylamine chromophore series and triphenylamine chromophore series reported to have the efficiency of ~7% (M.-S. Tsai *et al.*, 2007), ~6% (Z. Ning *et al.*, 2008) and ~5% (D. P. Hagberg *et al.*, 2007). They are considered to reach 45-70% with respect to that of an N719 metal dye-based device fabricated under the similar condition.

Moreover, the combination of π-conjugated polymers with inorganic semiconductors such as TiO_2 is of interest because the former can be the sensitizer and hole transport medium. Recently, oligo(2,5-pentyloxy-phenylenevinylene) carboxylic acid, DPO-OPV3-COOH (see Figure 7(a)), were synthesized and used in hybrid solar cells to enhance adsorption ability at the TiO_2 surface (P. A. van Hal *et al.*, 2003). The incident photon-to-electron conversion efficiency (IPCE) was reported to be 55% at the maximum absorption.

In addition, several theoretical works were presented to investigate physical and chemical properties of polymer (Karpfen *et al.*, 1991 and Chandross *et al.*, 1994). Theoretical quantity for making a direct comparison with experimental band gap is the transition (or excitation) energy from the ground state to the first dipole-allowed excited state. The implicit assumption underlying this approximation is that the lowest singlet excited state can be described by only one singly excited configuration in which an electron is promoted from Highest Occupied Molecular Orbital (HOMO) to Lowest Unoccupied Molecular Orbital (LUMO). Moreover, the HOMO-LUMO energy difference is an estimation of the transition energy since the latter contains significant contributions from two-electron integrals. However, the real situation is an accurate description of the lowest singlet excited state from a linear combination of a number of excited configurations, although the one mentioned above often plays a dominant role. The calculated HOMO-LUMO gap agrees fairly well with experimental band gap in many cases. It is probably due to the error cancellations (Nguyen *et al.*, 1989 and Swanson *et al.*, 1991). Hence, more rigorous information on the nature of the excited state is desired to obtain with other elaborate methods. A variety of theoretical approaches is used for evaluating the quantity for oligomers as well as infinite polymers. The crudest estimation is the orbital energy difference obtained from Hartree-Fock (HF) or density functional theory (DFT) calculations. Among those theories, HF-based methods such as configuration interaction singles (CIS) (Foresman *et al.*, 1992) and the random phase approximation (RPA) which is equivalent to the time-dependent HF (TD-HF) (Jamorski *et al.*, 1996 and Bauernschmitt *et al.*, 1997, 1998), usually provide qualitative or semi-quantitative descriptions for only low-lying excited states. Time-dependent DFT (TD-DFT) (Cai and Reimers, 2000 and Wiberg *et al.*, 2002) is recently developed for calculating excitation energies (Runge *et al.*, 1984; Bauernschmitt and Ahlrichs, 1996; Petersilka *et al.*, 1996; Stratmann *et al.*, 1998 and Seibert *et al.*, 2002). Its advantage over HF-based methods has been demonstrated with roughly comparable computational cost (Hirata *et al.*, 1999).

In this study, electronic properties, charge transfer, and effect of spacers and anchors group of the sensitizers of oligo(2,5-pentyloxy-phenylenevinylene) carboxylic acid (DPO-OPV3-COOH) and its derivatives were theoretically investigated because the intrinsic properties of the polymeric semiconductors have been widely studied increase well-defined π-conjugated oligomers. Quantum-chemical calculations were applied to obtain geometrical parameters and electronic properties. Investigation on the methods and basis set dependence of excitation energies calculated with TD-DFT method was also performed with the B3LYP functional to consider the chain-length dependence of the vertical excitation energies. The results were then compared with experimental data. Molar extinction coefficients were analyzed from the calculated oscillator strength. The benefits of these works lead to the guidance of efficiency-improved sensitizers of DSSCs.

The most commonly used dyes in photoelectrochemical applications are anchored to metal oxide via carboxylic acid, phosphonic acid or thiocyanic acid. The anchor groups can be used to bind various molecules to TiO_2. The carboxylic acid anchor groups appear to give an exceptionally good electronic coupling across the dye-semiconductor interface (J. Schnadt *et al*., 2002). Moreover, spacer groups can be introduced between the chromophore and the anchor group. It separates the chromophore and semiconductor and to control the electronic interactions between the dye and the nanoparticle (J. B. Asbury *et al*., 2000).

Various alkoxy substituents were selected to investigate the effect of spacer and anchor groups (Figure 8) on geometrical structures and electronic properties of the DPO-OPV3-COOH derivatives. The properties of the polymers were obtained from quantum chemical calculations. From the ground state geometries, electronic transitions of oligomers were achieved by TD-DFT calculation with the B3LYP functional to investigate the electron excitation absorption wavelength, and energy states. These information leads to the new design of sensitizers for the DSSCs.

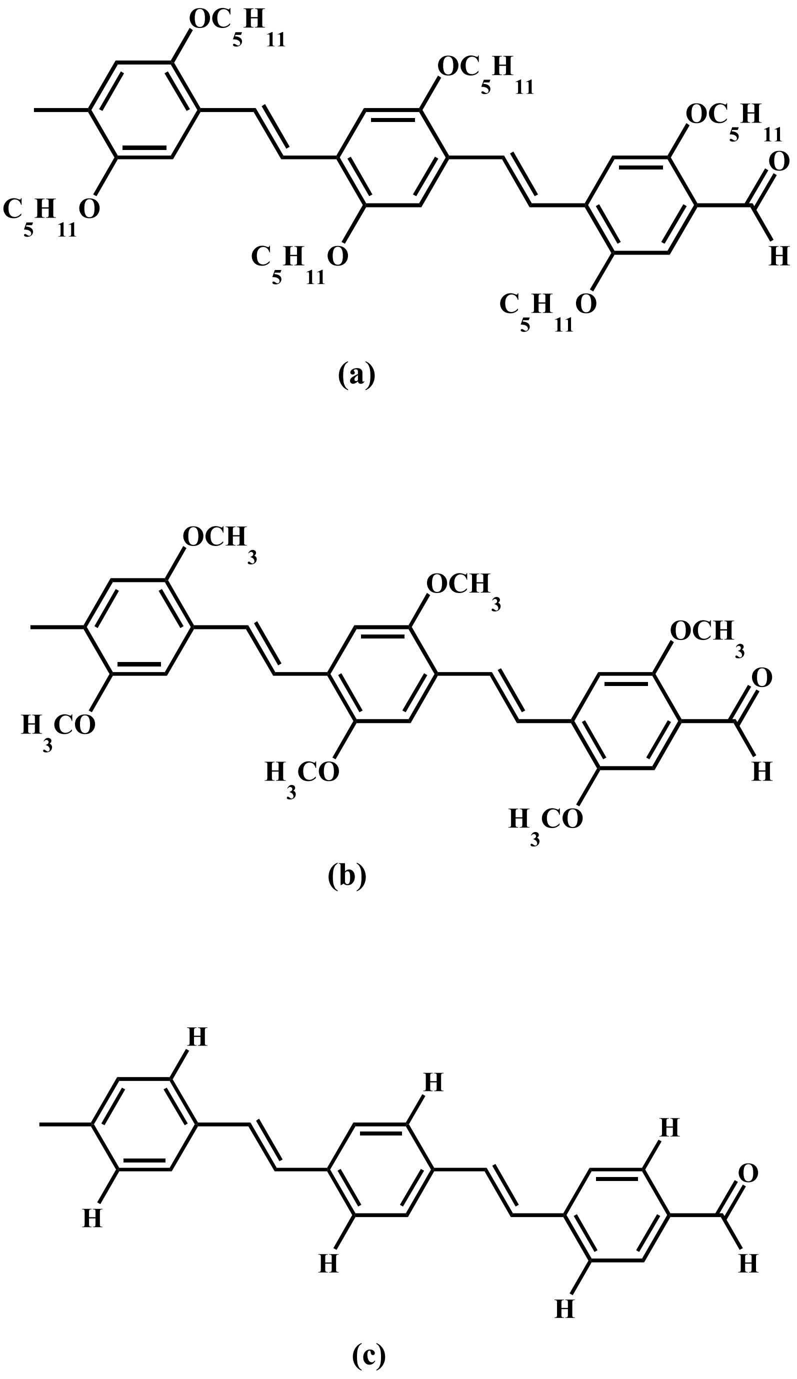

Figure 7 Chemical structures of DPO-OPV3-COOH and its alkoxy derivatives (a) oligo(2,5-pentyloxy-phenylenevinylene) carboxylic acid (DPO-OPV3-COOH) : R1=R2=O-CH_2-$CHCH_3$-C_2H_5, (b) oligo(2,5-methoxy-PPV3) carboxylic acid (DMO-OPV3-COOH), and (c) oligo(2,5-phenylenevinylene) carboxylis acid (OPV3-COOH)

(a) spacer groups

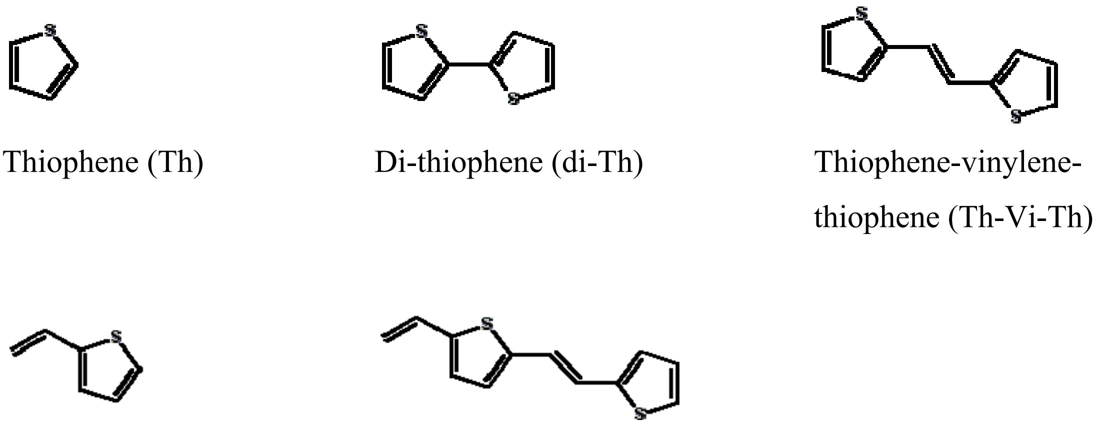

Thiophene (Th)

Di-thiophene (di-Th)

Thiophene-vinylene-thiophene (Th-Vi-Th)

Vinylene-thiophene (Vi-Th)

Di-vinylene-thiophene (di-Vi-Th)

(b) anchor groups

Cyanoacitate

Carboxylic

Figure 8 Chemical structures of (a) spacer groups and (b) anchor groups

LITERATURE REVIEW

The absorption of molecular dyes on the semiconductor surface results in the sensitization to visible light. The mechanism for the energy conversion of solar to electrical and chemical energy in DSSCs has been widely studied the conversion efficiencies of about 10% for such devices were studied in nanocrystalline titanium dioxide (TiO_2) and metal complex sensitizer dyes by Gratzel *et al*. (1991). From the study, the limited availability of these dyes together with their undesirable environmental impact has led to the search for cheaper and safer organic based dyes.

The efficiencies of DSSCs are found to be lower than these of the p-n junction solar cells. However, several research groups are interested in the development of sensitizers. For example, the design and synthesis of a new dye compounds whose isolated absorption spectrum, adsorption on semiconductor, electronic transition, and other properties were studied with both experiments and theoretical approaches.

Greg Smestad (1994) performed the detailed balance calculations on the DSSCs to find the particular optical absorption and the luminescence efficiency, or fluorescence yield to analyze an upper limit for the solar conversion efficiency of the finished cell. Even these models cannot predict the actual efficiency directly, they may serve as a guide for the actual open-circuit voltages (V_{oc}) and solar conversion efficiencies. The results indicate that at least 10% conversion efficiency with voltages of over 1 V can be produced from Ru trinuclear complexes.

Huang *et al*. (1997) studied the charge recombination between nanocrystalline TiO_2 electrodes and the I_3^-/I^-. The sensitizer was $[RuL_2(NCS)_2]$ (L = 2,2'-bipyridyl-4,4'-dicarboxylic acid). An apparent inequality between the dark current and the recombination current is ascribed to a voltage shift caused by a potential drop at the SnO_2/TiO_2 interface, ohmic losses in the SnO_2 and TiO_2, and overpotential for the redox reaction at the Pt counter electrode. Treating the dye-coated TiO_2 electrodes with pyridine derivatives (4-*tert*-butylpyridine, 2-vinylpyridine and poly(2-vinylpyridine)) improves significantly both V_{oc} (from 0.57 to 0.73 V) and the conversion efficiency (from 5.8 to 7.5%) at a radiant power of 100 mW/cm^2 (AM 1.5) with respect to the untreated electrode. Studies of the dye-covered electrodes show that the rate of recombination is the second order in I_3^- concentration, which is attributed to the disputations reaction of $2I_2^- \rightarrow I_3^- + I^-$ with I_2 as the electron acceptor in the back-reaction. Mass-transport theory is applied to understand the dependence of the short-circuit photocurrent on the radiant power at low I_3^- concentration and to calculate the diffusion coefficient of I_3^- ions (7.6 x 10^{-6} cm^2/s) in the porous TiO_2 structure. The dependence of other cell parameters on the concentration is also investigated.

Ehret *et al*. (2001) reported new chromophores explored for use in DSSCs. The attachment of various di-carboxylated cyanine dyes to nanocrystalline TiO_2 was examined spectroscopically and through their performance in a sensitized solar cell. It was found that aggregated forms of these cyanine dyes sensitized with an efficiency equal to that of the monomeric form and that combinations of cyanine dyes could be used to sensitize solar cells over the entire visible spectrum.

Nazeeruddin *et al*. (2005) presented a new series of panchromatic ruthenium(II) sensitizers derived from carboxylated terpyridyl complexes of tris-thiocyanato Ru(II). Black dye containing different degrees of protonation $\{(C_2H_5)_3NH\}[Ru(H_3tcterpy)(NCS)_3]$ 1, $\{(C_4H_9)_4N\}_2[Ru(H_2\ tcterpy)(NCS)_3]$ 2, $\{(C_4H_9)_4N\}_3[Ru(Htcterpy)(NCS)_3]$ 3, and $\{(C_4H_9)_4N\}_4[Ru(tcterpy)(NCS)_3]$ 4 (tcterpy = 4,4′,4″-tricarboxy-2,2′:6′,2″-terpyridine) have been synthesized and fully characterized by UV-vis, emission, IR, Raman, NMR, cyclic voltammetry, and X-ray diffraction studies. The crystal structure of complex 2 confirms the presence of a $Ru^{II}N6$ central core derived from the terpyridine ligand and three N-bonded thiocyanates. The low-energy metal-to-ligand charge-transfer absorption band showed marked solvatochromism due to the presence of thiocyanate ligands. The Ru(II)/(III) oxidation potential of the black dye and the ligand-based reduction potential shifted cathodically with decreasing number of protons and showed more reversible character. The dye has yielding over 80% IPCE. Solar cells containing the dye were subjected to determine their solar-to-electric conversion efficiency under the standard sunlight. A short circuit photocurrent density (I_{sc}) obtained was 20.5 mA/cm^2, and the V_{oc} was 0.72 V corresponding to an overall efficiency of 10.4%.

In 2005 this group reported a combined experimental and computational study of several ruthenium(II) sensitizers originated from the [Ru(dcbpyH$_2$)$_2$(NCS)$_2$], N3, and [Ru(dcbpyH$_2$)(tdbpy)(NCS)$_2$], N621, (dcbpyH$_2$ = 4,4'-dicarboxy-2,2'-bipyridine, tdbpy = 4,4'-tridecyl-2,2'-bipyridine) complexes. A purification procedure was developed to obtain pure N-bonded isomers of both types of sensitizers. The photovoltaic data of the purified N3 and N621 sensitizers adsorbed on TiO$_2$ films in their monoprotonated and diprotonated state, exhibited remarkable power conversion efficiency about 11.18 and 9.57%, respectively.

From these works, DSSCs with Ru bipyridyl complexes (N3 and N719, see Figure 4 and 5) and the black ruthenium dye as photosensitizers have achieved power conversion efficiencies up to 11.2% and 10.4%, respectively. However, the Ru transition metal is a limited resource and expensive. To obtain a cheaper one, metal-free organic photosensitizers are strongly desired. Metal-free organic dyes offer superior molar extinction coefficients, low cost, and a diversity of molecular structures. The organic photosensitizers can be coumarin, merocyanine, cyanine, indoline, hemicyanine, triphenylamine, dialkylaniline, bis(dimethylfluorenyl) aminophenyl, phenothiazine, tetrahydroquinoline, and carbazole.

Hara *et al.* (2002) developed novel coumarin dyes for use in the DSSC of nanocrystalline TiO$_2$. The absorption spectra of these dyes were remarkably red-shifted in the visible region from the conventional dye. Introduction of a methine unit (-CH=CH-) connecting both cyano (-CN) and carboxyl (-COOH) groups into the coumarin framework expanded the π-conjugation in the dye and thus resulted in a wide absorption. The novel dyes performed as efficient photosensitizers. The monochromatic IPCE from 420 to 600 nm for a DSSC based on NKX-2311 was over 70% with the maximum of 80% at 470 nm, which is almost equal to that obtained from the N3 dye system.

A quantitative understanding of molecular electronic excited states is important in many domains, including spectroscopy, photochemistry, and the design of optical materials. The prediction or interpretation of the discrete part of the spectrum is a demanding task for theoretical methods, especially for medium and large size molecules of chemical interest. Thus, an inexpensive yet accurate method for calculating vertical excitation energies would be very useful.

DFT has been remarkably successful at providing means for computing a variety of ground state properties with an accuracy which rivals that of post-HF methods. Indeed, the accuracy of current DFT models is at least comparable to the results obtained by low-order many body perturbation techniques, such as the second order Møller-Plesset (MP2) approach. Since DFT methods rectify many problems of the HF approximation at comparable computational cost, there is currently great interest in extending the DFT approach to excited electronic states. Time dependent generalization of the DFT theory offers a rigorous route to the calculation of the dynamic response of the charge density. Combining this with linear response theory allows the calculation of vertical electronic excitation spectra. The theoretical quantity for direct comparison with experimental band gap should be the transition (or excitation) energy from the ground state to the first dipole-allowed excited state. A variety of theoretical approaches can be a tool to evaluate this quantity for both oligomers and infinite polymers.

Tsai *et al.* (2007) synthesized and investigated the series of organic dyes based on 1*H*-phenanthro[9,10-*d*]imidazole chromophores in DSSCs. The dyes as the sensitizers exhibited good efficiencies, from 2.95 to 4.68%, which reached 45-70% with respect to that of an N719-based device fabricated under similar conditions. The B3LYP/6-31G* optimized ground state geometries were used. The TD-DFT calculated excitation energies were compared with the experimental data of UV-visible absorption and photocurrent-voltage characteristics. The TD-DFT result agrees with the charge-transfer character of the compounds and consistent with the device. The results indicated that the extent of charge separation in the excited state is an important factor for DSSC efficiency.

Ning *et al.* (2008) reported the synthesis and photophysical and electrochemical properties of a series of novel starburst triarylamine-based organic dyes. The starburst triarylamine group and the cyanoacetic acid take the role of electron donor and electron acceptor, respectively. It was found that the introduction of the former to form the D-D-π-A configuration brought about superior performance over the simple D-π-A configuration, in terms of bathochromically extended absorption spectra, enhanced molar extinction coefficients and better thermo-stability. Moreover, the HOMO and LUMO energy levels tuning can be conveniently accomplished by alternating the donor moiety, which was confirmed by electrochemical and theoretical calculations. DSSCs based on the one dye of their series showed the best photovoltaic performance: a maximum monochromatic IPCE of 85%, I_{sc} of 13.8 mA cm^{-2}, V_{oc} of 0.63 V, and a fill factor (ff) of 0.69, corresponding to an overall conversion efficiency of 6.02% under 100 mW/cm^2 irradiation. This work suggested that the dyes based on starburst triphenylamine donor are the promising candidates for the improvement of the performance of DSSCs.

Zhang *et al.* (2008) presented that DFT and TD-DFT calculations have been applied to study the coumarin dyes which act as photosensitizer in DSSCs. The absorption spectra of the dyes in ethanol can be well reproduced with theoretical method. The outstanding performance of NKX-2311 roots in higher light harvesting efficiency and more efficient electron injection efficiency into conduction band of TiO_2 electrode according to our computation. Referring to the conclusions, the new coumarin dyes were designed to possess the higher efficiency.

Hal *et al*. (2003) reported the interaction of an acid-functionalized oligo(*p*-phenylenevinylene) (OPV3-COOH) with nanocrystalline TiO_2 studied as a model for semiconducting polymer–inorganic material hybrid solar cells. Photoluminescence quenching and near steady-state photoinduced absorption spectroscopy demonstrate that an efficient forward photoinduced electron transfer occurs from OPV3-COOH to TiO_2. PV cells based on OPV3-COOH/nc-TiO_2 and a liquid electrolyte as a medium for hole transport provide an IPCE of 55%, comparable to the values obtained with the best ruthenium dyes.

Suramitr *et al*. (2003) studied the structures and electronic properties of the alkoxy derivertives of poly(1,4-phenylenevinylene) by using theoretical methods. A conformational study of alkoxy derivatives of poly(1,4-phenylenevinylene) by AM1, HF/3-21G and HF/6-31G calculations demonstrated that these derivatives have coplanar structure due to the formation of weak hydrogen bonds between the oxygen atom of the substituted alkoxy group and the hydrogen atom of the vinylene linkage. The excitation energy of polymers were calculated by using TD-DFT with B3LYP/6-31G and B3LYP/6-31G* levels. The extrapolated band gaps obtained from HOMO-LUMO energy difference from TD-DFT calculation of E_g(DMO-PPV) = 2.10 eV and E_g(MEH-PPV) = 2.08 eV, are excellent agreement with experimental data of E_g(DMO-PPV) = 2.18 eV and E_g(MEH-PPV) = 2.10 eV. The TDDFT calculation is assumed to give a good prediction for the excitation energy.

METHODS OF CALCULATION

1. Ground state calculations

The starting geometries of the oligomers were constructed by GaussView 3.0 program. The oligo(2,5-phenylenevinylene)carboxylic acid (OPV3-COOH) structure was fully optimized and modified by introducing alkoxy groups attached onto the phenylene ring at the ortho-carbons. Then, all quantum chemical calculations with *ab initio* and density functional theory (DFT) methods were carried out by the GAUSSIAN03 program**,** in order to study many properties and reactions of these molecules. The ground state chromophore models of sensitizer studied in this work are shown in Figure 7 and spacer and anchor groups in Figure 8.

The structures were fully optimized by using DFT method with B3LYP hybrid functional and *ab initio* with Hartree-Fock (HF) and 2nd order Moller-Plesset Perturbation Theory (MP2) methods at 6-31G* level of basis set, respectively. Moreover, these oligomers were functionalized with spacers (Figure 8), which link between oligomers chromophore and carboxylic acid acceptor.

The structural results such as bond length, bond angle, and bond torsion angle will be compared to X-ray crystallography data (Finder *et al*., 1974 and Stalmach *et al*., 1999) with the mean relative errors that is then defined as

$$\sum_{i=1}^{n} \frac{\left|X_{Cal} - X_{Exp}\right|}{\left|X_{Exp}\right|} \Big/ n \text{ ------ (7)}$$

For conjugated molecular system, the structures were often described by bond length alternation (BLA) value (Lagowski *et al.*, 2002), which is defined to distinguish the single and double bonds. In this work, BLA for phenylenevinylene of DPO-OPV3-COOH (See labeled numbers in Figure 10) were defined as follow

$$\begin{aligned} \mathrm{BLA} = {} & 2[(\mathrm{C2\text{-}23}) + (\mathrm{C5\text{-}C6})] \\ & - [(\mathrm{C1\text{-}C2}) + (\mathrm{C3\text{-}C4}) + (\mathrm{C4\text{-}C5}) + (\mathrm{C1\text{-}C6})] \\ & + [(\mathrm{C4\text{-}C7}) + (\mathrm{C8\text{-}C9})] - 2(\mathrm{C7\text{-}C8}) \qquad \text{------(8)} \end{aligned}$$

1.1. IR frequencies of DPO-OPV3

The IR frequencies of DPO-OPV3, whose carboxyl group was reduced for the comparison with MEH-PPV, were inquired by HF/6-31G* and B3LYP/6-31G* methods. The calculated values were scaled by 0.9135 and 0.9806, respectively, taken from the database of frequency scaling factors for electronic structure model (Zheng *et al.*, 2007). The results could be compared to the IR experimental spectrum of MEH-PPV that bears the similar functional groups of DPO-OPV3.

1.2. Conformational analysis

The di(2,5-methoxy-phenylenevinylene) (DMO-OPV2) as shown in Figure 9 was investigated by partial optimizations, based on *ab initio* and DFT calculations at HF/6-31G* and B3LYP/6-31G* methods. These results were confirmed by MP2/6-31G*//HF/6-31G* and MP2/6-31G*//B3LYP/6-31G* levels, respectively, in conventional quantum chemical notation "single point//optimization level". According to the flexibility of this dimer molecule, relative potential energy of α torsion angle ($\angle$C3-C4-C7-C8) was also performed in Figure 9. The dihedral angle was varied with a step size of 15° from 0-360°.

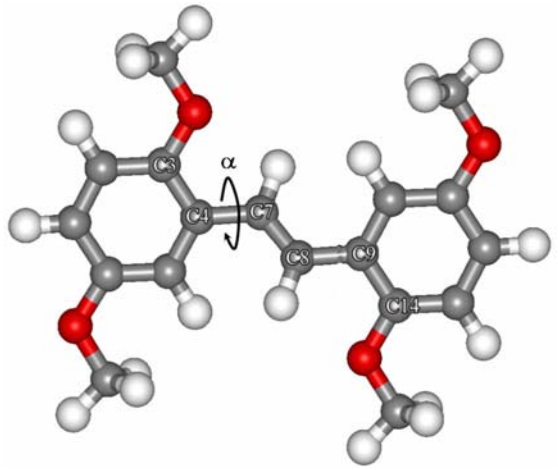

Figure 9 Schematic representation of the torsion angle focused in DMO-OPV2. α is defined as ∠C3-C4-C7-C8 torsion angle

2. Excited state calculations

The calculations of the excitation energies were then performed based on the ground state geometries. Methods and basis set dependence of excitation energies calculated with TD-DFT was also applied to investigate the OPV3-COOH and its derivatives, including functional oligomers with spacer and anchor groups. The calculations were used as the basis of TD-DFT calculations on the S_0 to S_1, S_2, and S_3 states of each molecule. TD-DFT calculations with the B3LYP functional on the all states of each molecule were carried out using the 6-31G* basis set in gas phase to investigate the chain length dependence of the vertical excitation energies of the compounds. The conductor polarizable continuum model (CPCM) is also conducted employing parameters and iterative computation methods (Zhang *et al*., 2008) to contain the solvation effect.

Single electronic spectra, absorption spectra, density of state (DOS), and charge distribution between the ground and excited states were obtained from TD-DFT data and calculated with GaussSum 2.0 (O,Boyle *et al*., 2005).

RESULTS AND DISCUSSION

1. Method validation

1.1. Comparison on the calculated ground state geometry parameters of DPO-OPV3-COOH by different theoretical methods with the experimental data

Yang *et al*. (2008) reported the full optimization of 2,5-diphenyl-1,4-distyrylbenzene (DPDSB) using the B3LYP functional and HF method at different level of basis sets: 6-31G and 6-31G*. It was found that the main geometrical parameters become closer to the experimental results with the upgraded basis set. The DPO-OPV3-COOH derivatives were therefore optimized with this basis set to study the structural parameters of ground state geometries and electronic transitions of the excited state structures.

The optimized geometrical parameters using the DFT approach with the B3LYP hybrid functional and the *ab initio* approach with HF method at 6-31G* basis set for DPO-OPV3-COOH (Figure 10), and MP2 method for DMO-OPV3-COOH (Figure 11) were presented in Table 1. The methoxy side chain groups were used in the representation for the penthoxy groups of DPO-OPV3-COOH to reduce the computational time of the MP2 optimization. Concerning phenylene groups, more steric hindrance at the side chains do not affect the convergence of the calculated structures. These calculated parameters of bond length and bond angle were found to agree with the X-ray crystallographic data reported by Finder *et al*. (1974) and Stalmach *et al*. (1999).

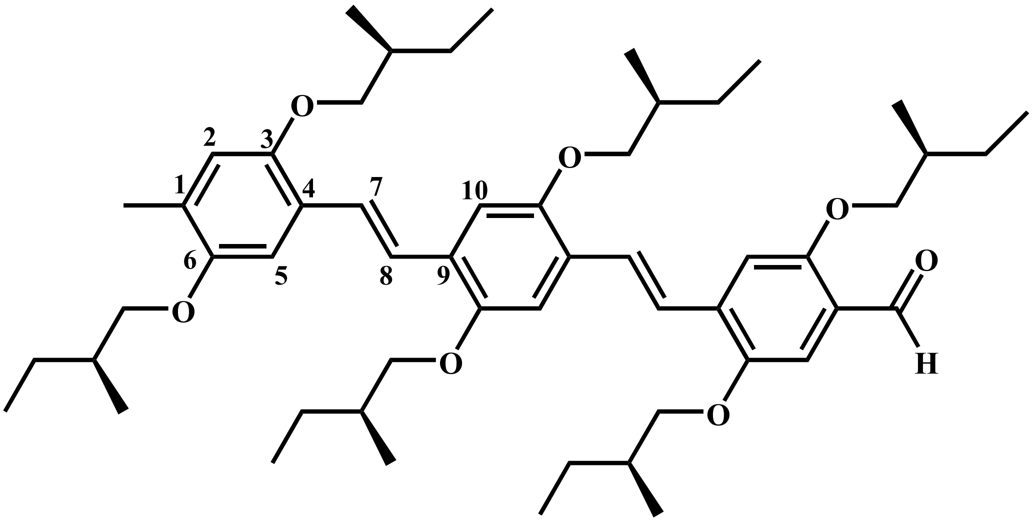

Figure 10 Schematic representation of DPO-OPV3-COOH. Labeled numbers are for the notation in this study.

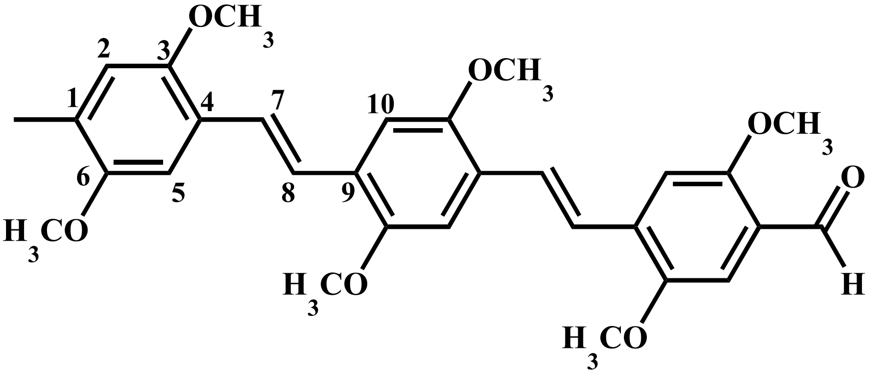

Figure 11 Schematic representation of DMO-OPV3-COOH. Labeled numbers are for the notation in this study

Table 1 Structural parameters of DPO-OPV3-COOH obtained from full optimization by HF and B3LYP methods, and DMO-OPV3-COOH from MP2 at 6-31G* level of basis set (Bond length in angstrom, Angle in degrees). BLA and the mean relative error values are also listed

Structural parameters	HF/6-31G*	B3LYP/6-31G*	MP2/6-31G*	X-ray
Bond length				
C1-C2	1.39	1.40	1.40	1.38[a]
C2-C3	1.39	1.40	1.40	1.39[a]
C3-C4	1.39	1.42	1.41	1.39[a]
C4-C5	1.40	1.41	1.41	1.40[a]
C5-C6	1.38	1.39	1.39	1.34[a]
C6-C1	1.40	1.42	1.41	1.37[a]
C4-C7	1.48	1.46	1.46	1.47[a]
C7-C8	1.33	1.35	1.35	1.32[a]
C8-C9	1.48	1.46	1.46	1.47[a]
Bond angle				
C3-C4-C7	125.8	126.7	124.2	125.3[b]
C4-C7-C8	124.4	126.0	124.0	125.3[b]
Torsion angle				
C4-C5-C7-C8	-25.5	-3.8	-28.5	-18.0[b]
C7-C8-C9-C10	30.7	6.9	28.7	18.0[b]
Relative error	0.0084	0.0185	0.0170	N/A
BLA	0.26	0.14	0.18	0.20

Sources: [a] Finder et al. (1974) and [b] Stalmach et al. (1999)

To simplify the geometries of phenylene ring of DPO-OPV3-COOH (Figure 10), its bond lengths are reported in an average value. From the mean relative errors (0.0084 and 0.0185) and the BLA (0.26 and 0.14) of the optimized ground state geometries obtained from HF/6-31G* and B3LYP/6-31G* methods, respectively, are in a good agreement with the crystallographic data. It is found that the key parameters become closer to the experimental results with the 6-31G* basis set.

The bond angle C3-C4-C7 and C4-C7-C8 in the HF/6-31G* (125.8° and 126.7°) and B3LYP/6-31G* (126.7° and 126.0°) optimized geometries are similar and comparable to the crystallographic data (125.3° and 125.3°), but the torsion angle C4-C5-C7-C8 and C7-C8-C9-C10 are different. From the investigation of torsion angles from the HF method (-25.5° and 30.7°), the DPO-OPV3-COOH structure can be considered to be coplanar by having both phenylene ring oppositely twisted with in about 30.0° from the planar configuration. Conversely, those from the B3LYP geometry optimization (-3.8° and 6.9°) are nearly 5°. The structure can be presented the planar configuration. In the solid state point of view, both coplanar and planar geometries of DPO-OPV3-COOH (shown in Figure 12) should be considered.

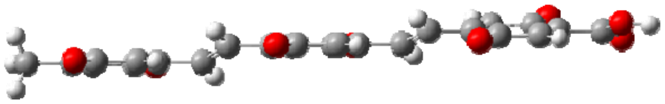

(a)

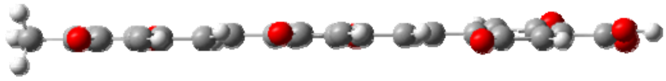

(b)

Figure 12 Side view of DPO-OPV3-COOH optimized structure. (a) coplanar configuration of the HF/6-31G* and (b) planar form of the B3LYP/6-31G* method

The different ground state geometries obtained from different theoretical methods are noteworthy because an accurate structure prediction leads to other reliable property calculations. The DPO-OPV3-COOH structure is therefore optimized using higher level method of calculation such as MP2 method. Side chains attached on its phenylene groups are reduced from pentoxyl (Figure 10) to methoxyl group (DMO-OPV3-COOH, shown in Figure 11).

The MP2/6-31G* optimized geometrical parameters for DMO-OPV3-COOH, bond length, bond angle, torsion angle, including BLA and relative error values, are presented in Table 1. It is found that bond length,bond angle (124.2 and 124.0), the BLA (0.18), and the mean relative error (0.017) of phenylenevinelene ring of the optimized structure are comparable to the X-ray crystallographic data. The torsion angles C4-C5-C7-C8 and C7-C8-C9-C10 are -28.5° and 28.7°, respectively. They are similar to that of the HF/6-31G* method. The phenylene ring is found the coplanar configuration (Figure 13), which corresponds to the reports by Suramitr *et al*. (2004).

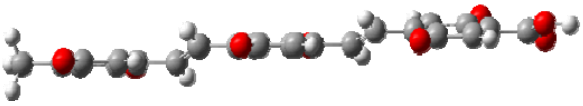

Figure 13 Side view of coplanar configuration of DMO-OPV3-COOH, optimized by MP2/6-31G* method

The reports of Suramitr *et al*. (2004) indicated the intramolecular hydrogen bonding between oxygen atom on alkoxy group and hydrogen atom at vinylene linkage was found in the poly(phenylenevinylene) derivatives. The interaction leads to the different configurations of these molecules. In this study, the coplanar structures obtain from HF and MP2 methods and planar structure obtained from B3LYP may be caused from the strength of intramolecular hydrogen bonding. Therefore, the hydrogen bond distance, the Mulliken charge distribution, and IR frequency were then investigated the intramolecular hydrogen bonding to confirm the configuration of the molecule.

1.2. Intramolecular hydrogen bonding in DPO-OPV3-COOH derivatives

The DPO-OPV3-COOH derivatives contain alkoxy group side chains attached at their ortho-position of the phenylene ring. Due to the steric effect, the structures should not be planar or coplanar. From the calculated torsion angles, DPO-OPV3-COOH geometries obtained from HF/6-31G* and B3LYP/6-31G* optimizations and DMO-OPV3-COOH geometry obtained from MP2/6-31G* method shown the existence of four intramolecular hydrogen bonding (IBD) between oxygen atom of substituents and the hydrogen atom at the vinylene linkage (O1-H1, O2-H2, O3-H3, and O4-H4) as in Figure 14. The IDB, often the formation of a weak bond between a hydrogen acceptor and a hydrogen donor, causes planarization in the organic molecules (Suramitr *et al.*, 2004). Our finding is supported by the work of Stalmach *et al.* (1999) in which reported the distance between oxygen and hydrogen atoms of more than 2.4 Å in the X-ray structures of several 2,5-dialkoxy-substitued PPV derivatives.

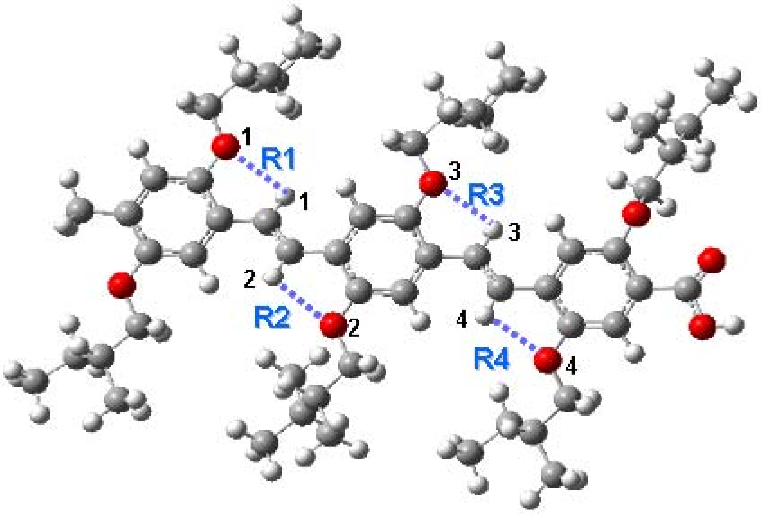

Figure 14 Intermolecular hydrogen bonding between oxygen atoms on alkoxy groups and hydrogen atoms at vinylene linkage in DPO-OPV3-COOH

As shown in Figure 14 and Table 2, the average IDB distance between the oxygen atoms on alkoxy groups and the hydrogen atoms at vinylene linkages are 2.43, 2.30 and 2.42 Å from the geometries optimized using HF/6-31G*, B3LYP/6-31G*, and MP2/6-31G* methods, respectively.

Table 2 Intramolecular bond distances of DPO-OPV3-COOH derivatives optimized using HF, B3LYP and MP2 methods with 6-31G* basis set

Bond	Distance (Å)		
	HF/6-31G*	B3LYP/6-31G*	MP2/6-31G*
R1	2.42	2.31	2.42
R2	2.45	2.30	2.42
R3	2.39	2.30	2.41
R4	2.46	2.31	2.42
Average	2.43	2.30	2.42

The results from three optimized structures indicate that the average distance of R(O-H) about 2.40 Å is in the range of weak intramolecular hydrogen bonding. From the planar structure of B3LYP/6-31G* optimization, R(O-H) being 2.30 Å is shorter than that of coplanar structures of HF/6-31G* and MP2/6-31G*. Therefore, the structure obtained from B3LYP/6-31G* optimization has a stronger intramolecular hydrogen bonding than the others.

1.3. The Mulliken charge distribution

From the report of Sun *et al.* (2007), the IDB was found between hydrogen atom at –OH group and nitrogen donor atom in enol planar form of 2-(2’-hydroxy phenyl)benzothiazole (Figure 15(a)), not in the twisted form, shown in Figure 15(b), because of the orientation of hydrogen atom of the -OH group. The difference of the Mulliken charge on nitrogen donor atom between that of the enol and the normal forms are different. The IDB causes the increase of negative charge on nitrogen atom at normal form to enol form. Consequently, the planarization is noted for the configuration.

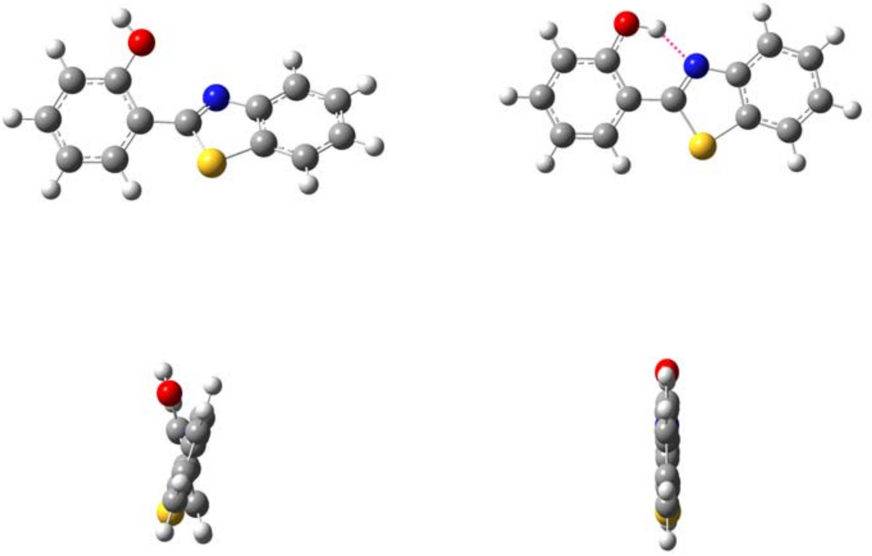

(a) **(b)**

Figure 15 Top and side views of 2-(2’-hydroxy phenyl)benzothiazole at (a) the normal and (b) enol forms obtained by B3LYP/6-31G** geometry optimizations

Source: Sun *et al.* (2007)

For DPO-OPV3-COOH in this study, The Mulliken charge on oxygen and hydrogen atoms, affected by intermolecular hydrogen bonding, were calculated with HF and B3LYP methods and in DMO-OPV3-COOH calculated with MP2 method are listed in Table 3. The average charges on these oxygen atoms calculated with HF/6-31G*, B3LYP/6-31G*, and MP2/6-31G* methods are -0.693, -0.540, and -0.678 and those of hydrogen atoms are 0.215, 0.154, and .220, respectively.

Table 3 The Mulliken charges on oxygen atoms on alkoxy groups and hydrogen atoms at vinylene linkage calculated with various methods (see labeled atom in Figure 14)

Label atom	Mulliken charge		
	HF/6-31G*	B3LYP/6-31G*	MP2/6-31G*
O1	-0.692	-0.537	-0.677
O2	-0.693	-0.539	-0.679
O3	-0.695	-0.542	-0.678
O4	-0.694	-0.539	-0.676
Average	-0.693	-0.540	-0.678
H1	0.213	0.153	0.216
H2	0.210	0.151	0.218
H3	0.223	0.160	0.225
H4	0.213	0.151	0.220
Average	0.215	0.154	0.220

The Mulliken charges of planar structure from the B3LYP optimization are less negative than those of the coplanar structures from HF and MP2 optimizations. It suggests that the smaller R(O-H) and less negatively charge on oxygen atoms of DPO-OPV3-COOH planarization observed in the B3LYP optimized structure indicate stronger intramolecular hydrogen bonding than the larger R(O-H) and more negative charge of the coplanarization in HF and MP2 optimized structures.

1.4. IR spectrum calculation for DMO-OPV3

The study of Matsuura and co-workers (2003) shows that an intramolecular C-H···O interaction in the 1-methoxy-2-(dimethylamino)ethane (MDAE) (Figure 16) leads to a blue-shift of the stretching vibration frequency (wavenumber) of this bond, due to the C-H bond contraction. The results were also observed with both infrared spectroscopy and computational calculation.

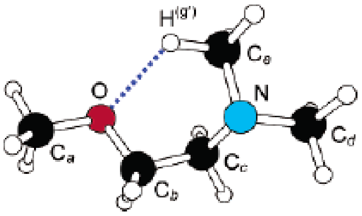

Figure 16 Optimized structure of MDAE by using B3LYP/6-311+G** level. C_a-H···O hydrogen bonding is presented with a dotted line

Source: Matsuura *et al.* (2007)

In this study, IR spectra of DPO-OPV3 (see the structure in Figure 17), whose carboxyl group was reduced to comparison with MEH-PPV frequency results, were investigated to confirm the IBD in different configuration structures. The calculated frequencies scaling factor of 0.9135 and 0.9806 were used to adapt the more accurate value for HF/6-31G* and B3LYP/6-31G* calculations, respectively. The calculated spectra were compared to the experimental one. They were found to be consistent with the FTIR experimental spectrum of MEH-PPV by Posudievsky *et al.* (2006) (Figure 18). All vibrational modes were assigned.

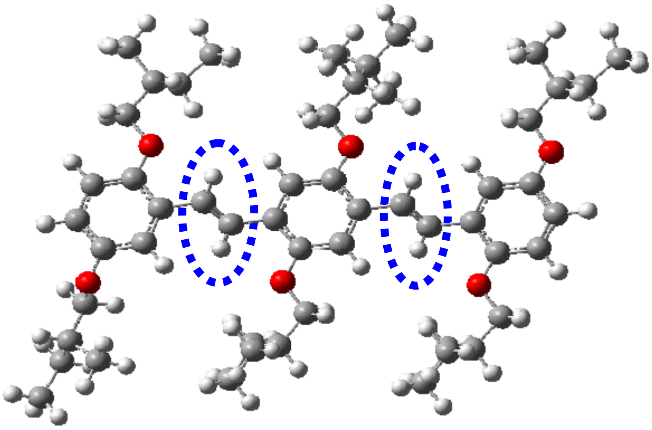

Figure 17 Chemical structure of DPO-OPV3 that was investigated IR spectra. The hydrogen atoms at vinylene likage are depicted by dotted lines

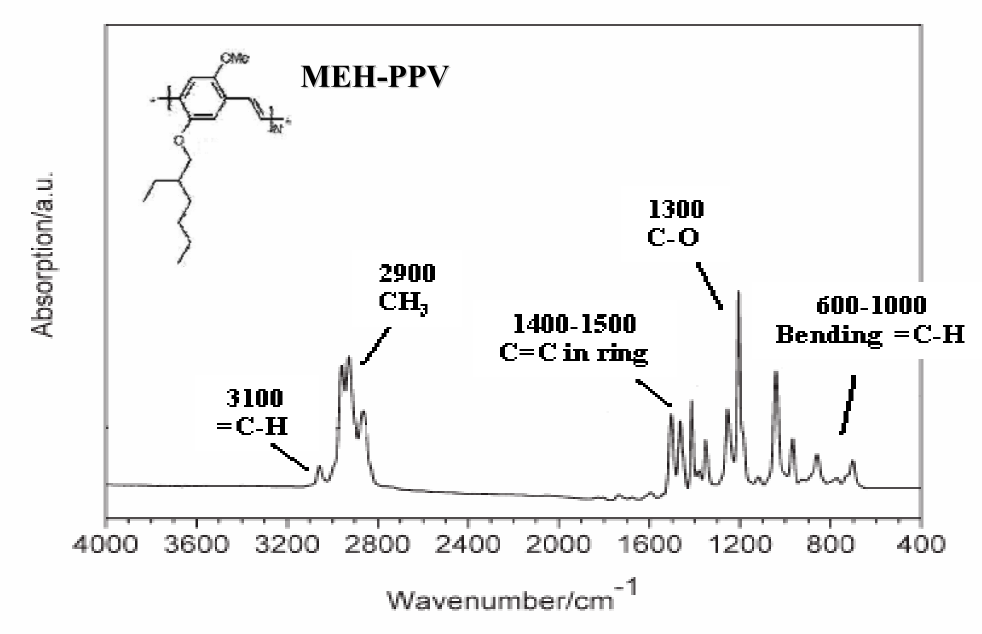

Figure 18 FTIR spectrum of MEH-PPV

Source: Posudievsky *et al.* (2006)

The IR spectra of the C-H stretching on vinylene linkage (see dotted line in Figure 17) predicted with HF/6-31G* and B3LYP6-31G* methods are shown in Figure 19. The wavenumber of 3128 cm^{-1} from HF/6-31G* calculation on the non-planar structure was found to be red-shifted from that the values of 3180 cm^{-1} from B3LYP/6-31G* prediction on the planar structure. The difference vibrational frequency obtained from different conformation indicated that the intramolecular interaction of oxygen atom on alkoxy group and hydrogen atom at vinylene linkage causes the red-shift in the vibrational mode since the interaction of oxygen atom and hydrogen atom of planar structure from B3LYP/6-31G* optimization is stronger than that of coplanar structure from HF/6-31G* one. The contraction of H-C=C bond at the vinylene linkage leads to higher wavenumber of C-H stretching.

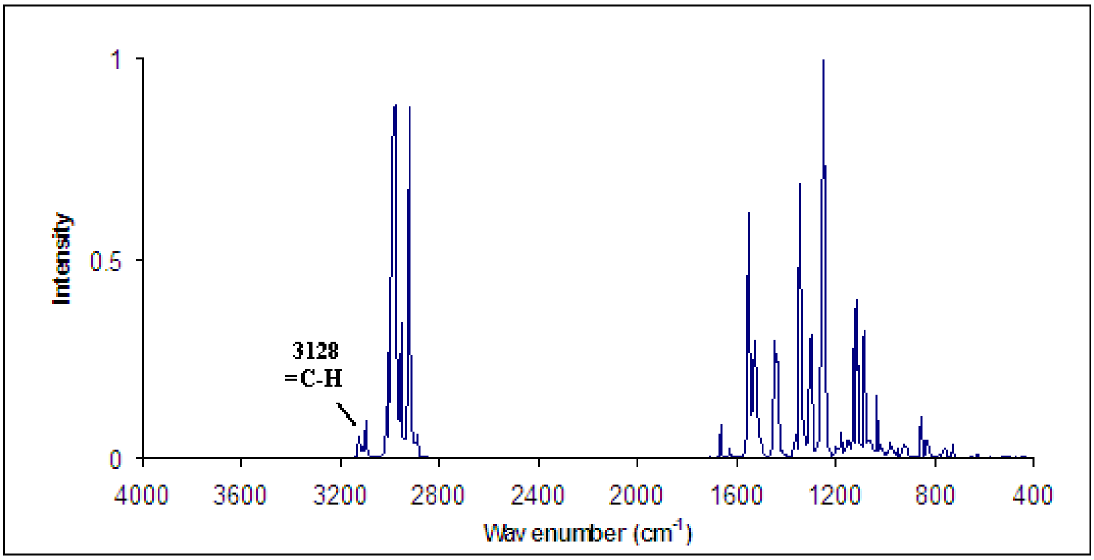

(a)

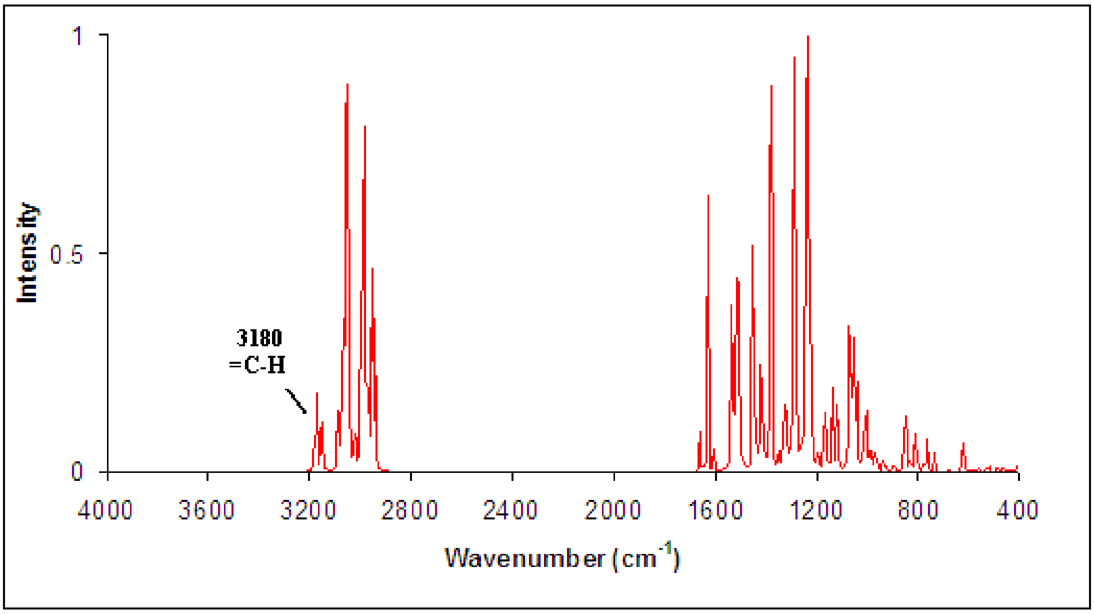

(b)

Figure 19 Calculated IR spectra of DPO-OPV3 where (a) were calculated with HF/6-31G* method and scaled by 0.9135 and (b) were calculated by B3LYP/6-31G* method and scaled by 0.9806

1.5. Conformational analysis

Potential energy for DMO-OPV2 with the change of α torsion angle (∠C4-C5-C7-C8) of vinylene unit was performed with HF/6-31G* and B3LYP/6-31G* methods, as shown in Figure 20. The former predicted that this oligomer prefers to be in non-planar conformation with the energy difference less than of 0.3 kcal/mol, whereas the difference is larger for B3LYP method.

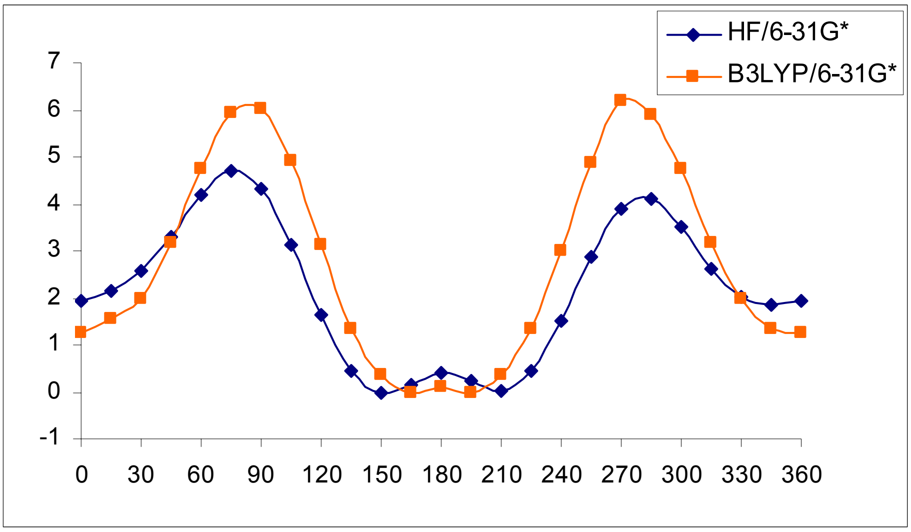

Figure 20 Potential energy surfaces for DMO-OPV2 with the change of α torsion angle (∠C3-C4-C7-C8) of vinylene unit obtained from HF/6-31G* and B3LYP/6-31G* calculations

MP2 single point calculations, noted as MP2/6-31G*//HF/6-31G* and MP2//B3LYP/6-31G*, were made to determine the potential energy of structures optimized with HF/6-31G* and B3LYP/6-31G* methods, respectively. The plots presented in Figure 21 supports the efficiency of the HF method to produce a similar potential energy curve with two minima at torsion angle around 150-210°. The results from both methods show that the non-planar conformation, in which two phenylene rings lie in parallel, is favored. In contrast, that of the result from DFT with B3LYP calculation shows only one minimum at the torsion angle of about 180°.

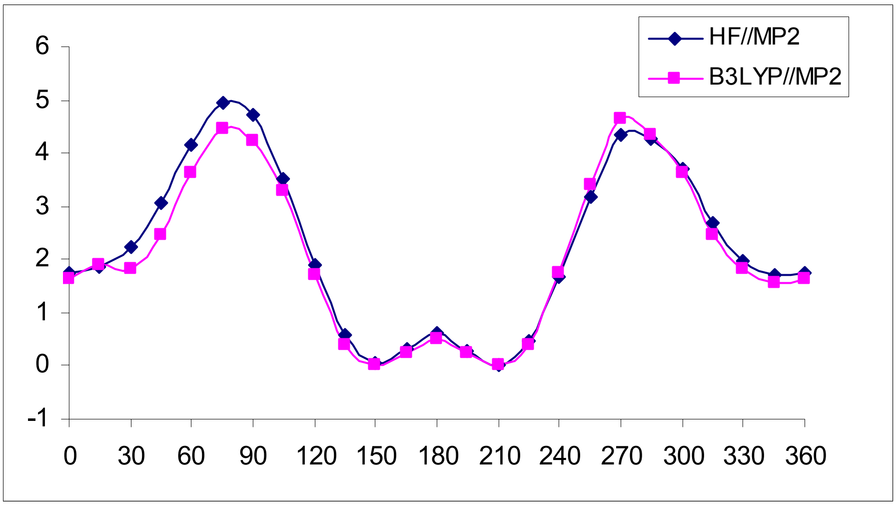

Figure 21 Potential energy surfaces for DMO-OPV2 with the α torsion angle (∠C3-C4-C7-C8) of vinylene unit predicted with MP2/6-31G*//HF/6-31G* and MP2//B3LYP/6-31G* method

From the calculated bond length, bond angle, bond torsion angle, R(O-H) distances, the Mulliken charge analysis, IR spectrum, and conformational analysis, we conclude that DPO-OPV3-COOH derivatives bears intramolecular hydrogen bonding between oxygen atoms on alkoxy groups and hydrogen atoms at vinylene linkage that causes the different configurations of the molecule.

1.6. Comparison on the electronic transition based on ground state geometries optimized with HF, B3LYP and MP2 methods

Electronic transitions of DPO-OPV3-COOH were investigated to confirm the configuration for ground state geometry optimized with different methods. Excitation energies and oscillator strengths for the transition from ground state (S_0) to first (S_1), second (S_2), and third singlet excited state (S_3) of the molecule was calculated using TD-DFT calculation in gas phase at the B3LYP/6-31G* level on HF/6-31G*, B3LYP/631G*, and MP3/6-31G* optimized ground state structures. Comparisons of the predicted values to the absorption band of this molecule in toluene (van Hal *et al*., 2003) were made in Table 4.

Table 4 Calculated transition for DPO-OPV3-COOH using TD-B3LYP/6-31G* method, compared to the experimental absorption wavelength in the toluene solvent

Ground state Geometry optimization	State	Excitation[a]	λ		f[b]
			nm	eV	
HF/6-31G*	$S_0 \rightarrow S_1$	H→L (67%)	412	3.00	0.960
	$S_0 \rightarrow S_2$	H-1→L (67%)	360	3.43	0.035
	$S_0 \rightarrow S_3$	H→L+1 (56%)	333	3.72	0.315
B3LYP/6-31G*	$S_0 \rightarrow S_1$	H→L (65%)	485	2.56	1.417
	$S_0 \rightarrow S_2$	H-1→L (65%)	397	3.11	0.084
	$S_0 \rightarrow S_3$	H→L+1 (52%)	370	3.35	0.034
MP2/6-31G*	$S_0 \rightarrow S_1$	H→L (66%)	430	2.88	1.117
	$S_0 \rightarrow S_2$	H-1→L (54%)	370	3.35	0.039
	$S_0 \rightarrow S_3$	H→L+1 (54%)	346	3.58	0.289
Absorption data[c]			430	2.88	

[a] H = HOMO, L = LUMO, H-1 = next highest occupied molecular orbital, or HOMO-1, and L1 = LUMO+1. [b] Oscillator strength. [c] van Hal *et al*. (2003)

In Table 4, TD-B3LYP calculations on all ground state geometries are used to predict the oscillator strength. It is found that the $S_0 \rightarrow S_1$ transition corresponding to the excitation from the HOMO to the LUMO is dominant. The absorption wavelengths of the transition obtained from the ground state geometries optimized using HF, B3LYP, and MP2 are 423, 485, and 430 nm, respectively. These results are in qualitative agreement with experimental absorption data. However, the wavelength of the structure from HF and MP2 methods are closer to experimental data of 430 nm than that of B3LYP method.

Table 5 Calculated transition for DPO-OPV3-COOH using TD-B3LYP/6-31G* method. The CPCM model was conducted to include the solvent effect of toluene to compare to the experimental absorption wavelength in the toluene solvent

Ground-state geometry optimization	State	Excitation	λ		*F*
			nm	eV	
HF/6-31G*	$S_0 \rightarrow S_1$	H→L (67%)	423	2.93	1.148
	$S_0 \rightarrow S_2$	H-1→L (68%)	367	3.38	0.036
	$S_0 \rightarrow S_3$	H→L+1 (58%)	336	3.68	0.334
B3LYP/6-31G*	$S_0 \rightarrow S_1$	H→L (66%)	509	2.43	1.648
	$S_0 \rightarrow S_2$	H-1→L (67%)	406	3.05	0.069
	$S_0 \rightarrow S_3$	H→L+1 (51%)	374	3.31	0.228
MP2/6-31G*	$S_0 \rightarrow S_1$	H→L (67%)	445	2.78	1.316
	$S_0 \rightarrow S_2$	H-1→L (67%)	375	3.30	0.023
	$S_0 \rightarrow S_3$	H→L+1 (58%)	349	3.54	0.289
Absorption data			430	2.88	

In Table 5, TD-B3LYP calculations including the solvation effect of toluene is performed on the ground state geometries those were optimized in the gas phase with HF, B3LYP, and MP2 methods and the 6-31G* basis set. The conductor polarizable continuum model (CPCM) was employed to take the toluene solvation effect into account. The absorption wavelengths of all geometries are red-shifted compared to those in which the effect is neglected.

The absorption spectra of these geometries from various methods were simulated with TD-B3LYP method combined with the inclusion of the solvent effect. Their simulated spectra are depicted in Figure 22. Our predicted absorption peaks, labeled in Figure 22, are found to correspond to the absorption peak observed in UV-vis spectrum (Figure 23). The compounds of DPO-OPV3-COOH (optimized with HF/6-31G* method) and DMO-OPV3-COOH (optimized with MP2/6-31G* method) are found to have the maximum absorption peaks at 423 and 445 nm, respectively.

The calculated value for the former is in better agreement with the observed one than that from B3LYP/6-31G* optimized structure at 509 nm.

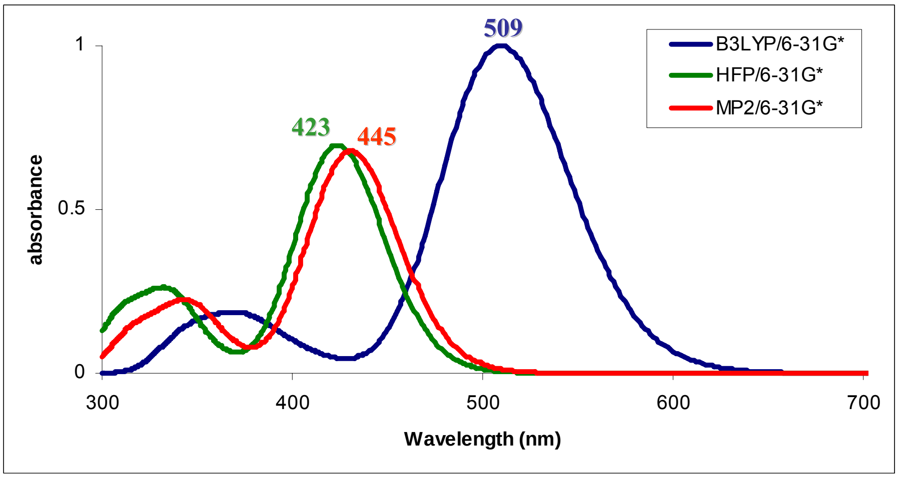

Figure 22 Comparison of simulated absorption spectra from different ground state geometry, optimized with combined TD-B3LYP/6-31G* method with CPCM to include the solvent effect of toluene

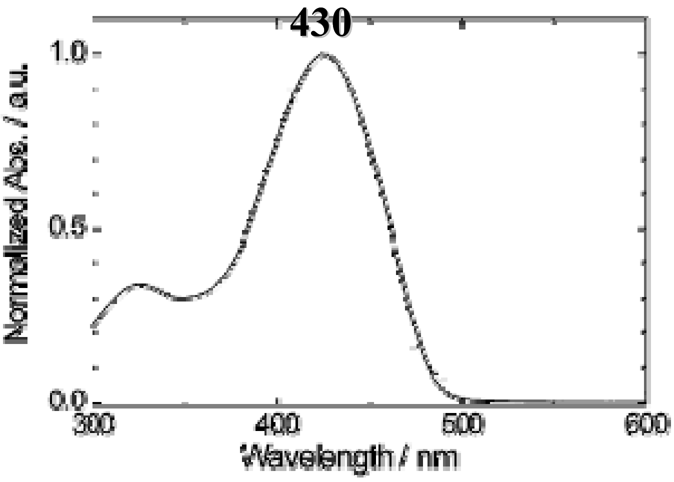

Figure 23 The experimental UV-visible spectrum of DPO-OPV3-COOH in toluene

Source: van Hal *et al*. (2003)

From our calculated electronic transitions with TD-B3LYP calculation compared with the experimental data, the results from the ground state geometries of DPO-OPV3-COOH derivatives using HF/6-31G* and MP2/6-31G* optimizations are in better agreement than B3LYP/6-31G* method. For the structure accuracy, the HF/6-31G* method is therefore selected for the ground state geometry optimization. The coplanar geometries were obtained to study the effect of spacer and anchor (or acceptor) groups of DPO-OPV3-COOH derivatives.

2. Excited state structure

2.1. Electronic properties of DPO-OPV3-COOH

HOMO and LUMO energy values for DPO-OPV3-COOH obtained from the HF/6-31G* optimized geometry were calculated at the TD-B3LYP/6-31G* level and presented in Figure 24. Judging from the LUMO value of -1.57 eV, the excited state energy levels are much higher than the bottom of the conduction band of TiO_2 of -4.40 eV. The results indicated that the electron injection process from the excited state of the compound to TiO_2 conduction band is viable.

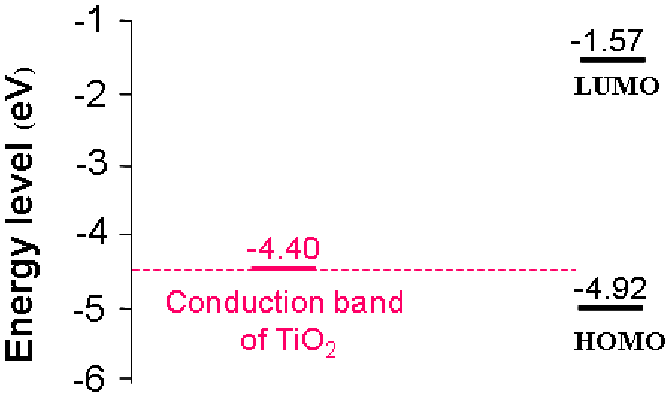

Figure 24 Calculated HOMO and LUMO energy levels for DPO-OPV3-COOH, compared with conduction band energy level of TiO_2

2.2. Molecular orbital of DPO-OPV3-COOH

The molecular orbitals of DPO-OPV3-COOH from the electronic transition results were examined with TD-B3LYP/6-31G* geometry optimization. The $S_0 \rightarrow S_1$ transition has the highest oscillator strength thus the most probable transition, corresponding to excitation from HOMO to LUMO as shown in Table 5. The HOMO-2, HOMO-1, HOMO, LUMO, and LUMO+1 are also depicted in Figure 25.

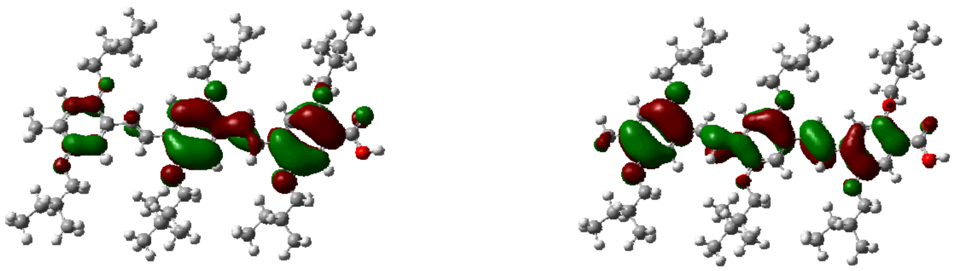

HOMO-2 HOMO-1

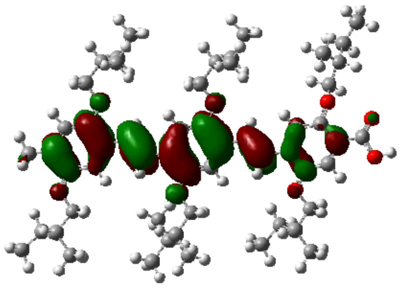

HOMO

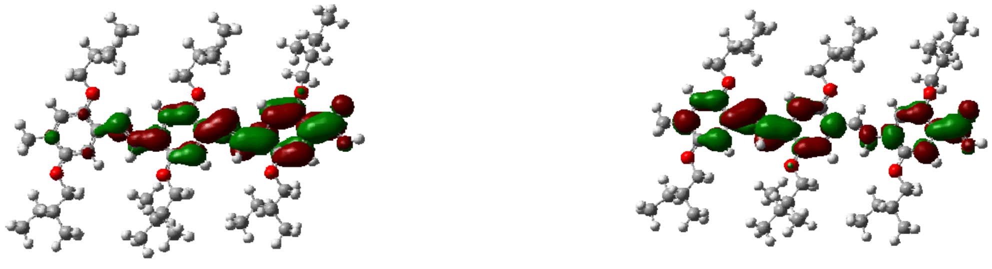

LUMO LUMO+1

Figure 25 The structures of frontier orbitals for DPO-OPV3-COOH

It can be identified that the absorption band of this compound is attributed to π→π* transition. The LUMO orbital possesses larger composition of carboxyl group located at the end of chromophore unit chain compared with the HOMO orbital which is liable to located at phenylenevinylene ring.

The electronic transition indicates that when electron at ground state is excited by photon from the sun light, electron would transfer from the phenylene ring (chromophore) towards the carboxyl group. Because DPO-OPV3-COOH is anchored onto the surface semiconductor (TiO_2) through carboxylic acid, electron injection process will be facilitated as the molecule is excited.

3. Effect of spacer and anchor groups

The models of oligo(2,5-pentyloxy-phenylenevinylene) (DPO-OPV3), oligo(2,5-pentyloxy-phenylenevinylene) carboxylic acid (DPO-OPV3-COOH), and oligo(2,5-pentyloxy-phenylenevinylene)thiophene carboxylic acid (DPO-OPV3-thi-COOH) were studied the effect of spacer and anchor groups as shown the ground state geometries in Figure 26. Carboxyl group (anchor) and thiophene (spacer) were constructed and optimized with the HF/6-31G* method. The electronic transition, absorption spectrum, and molecular orbital were calculated by TD-B3LYP/6-31G*.

First, the ground state geometries (Figure 26) are studied. The ground state geometries of DPO-OPV3 and DPO-OPV3-Th-COOH are similar to that of DPO-OPV3-COOH discussed in part 1. The conformation of these structures is coplanar, whose phenylene rings were oppositely twisted from planar angle.

The most probable transitions of all compounds, which account from its highest oscillator strength, are listed in Table 6. The oscillator strength of DPO-OPV3, DPO-OPV3-COOH, and DPO-OPV3-Th-COOH are 1.232, 1.148, and 1.221, respectively, corresponding to the $S_0 \rightarrow S_1$ (HOMO→LUMO) transition. The calculated absorption spectra of all compounds in toluene salvation effect were simulated and presented in Figure 27. From DPO-OPV3, DPO-OPV3-COOH to

DPO-OPV3-Th-COOH, the conjugated structures become larger although their phenylenevinylene chromophores are the same. It is indicated that the absorption spectra of all compounds were red-shifted from 394, 423, to 434 with the size expansion of their conjugate system.

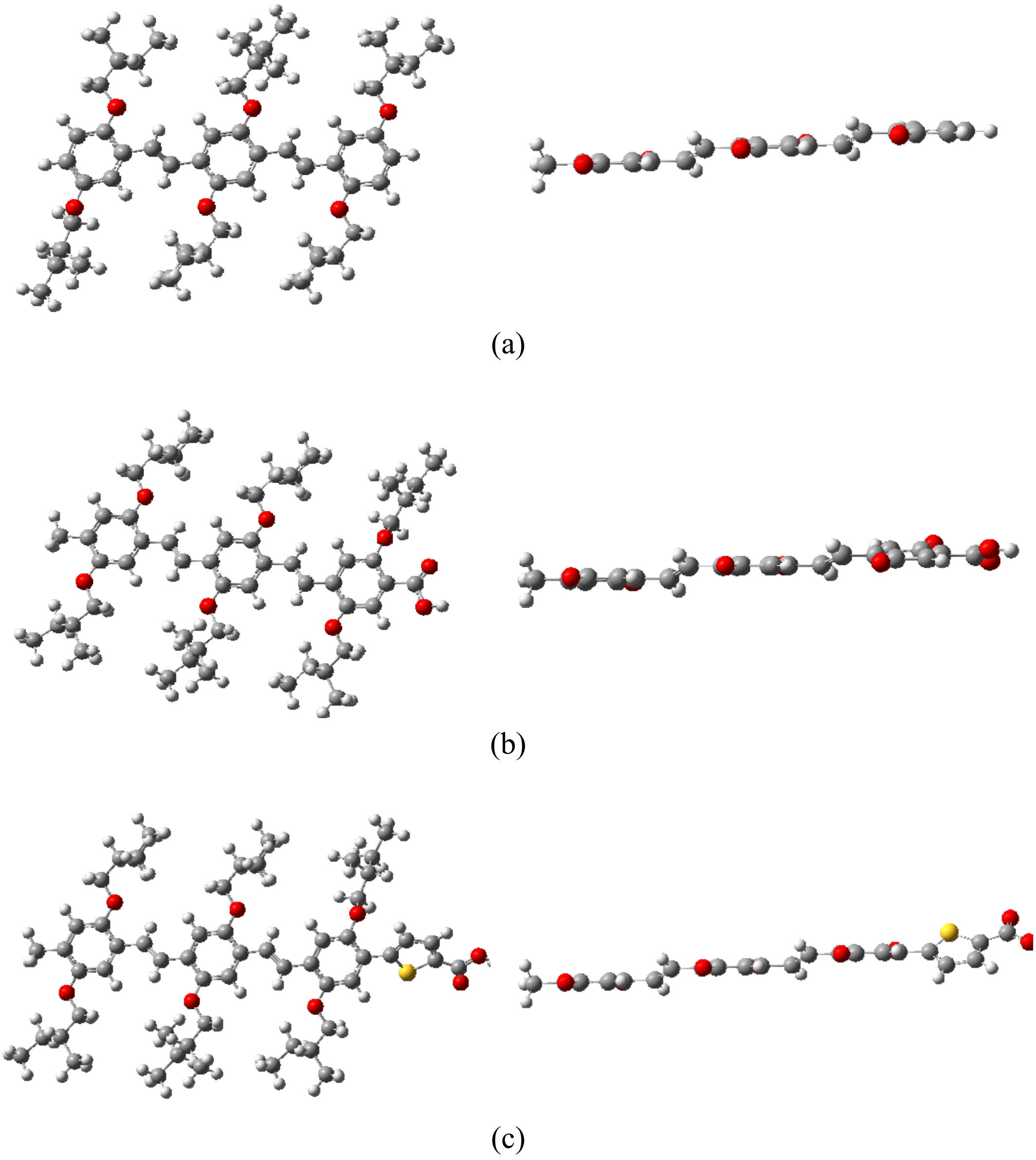

(a)

(b)

(c)

Figure 26 Top and side view of optimized structures (a) DPO-OPV3, (b) DPO-OPV3-COOH, and (c) DPO-OPV3-Th-COOH

Table 6 Calculated electronic transitions for DPO-OPV3, DPO-OPV3-COOH, and DPO-OPV3-Th-COOH using TD-B3LYP/6-31G*//HF/6-31G* method

Compounds	State	Excitation	λ_{cal}		*F*
			nm	eV	
DPO-OPV3	$S_0 \rightarrow S_1$	H→L (67%)	394	3.15	1.232
	$S_0 \rightarrow S_2$	H-1→L (68%)	345	3.59	0.005
	$S_0 \rightarrow S_3$	H-2→L (58%)	323	3.84	0.106
DPO-OPV3-COOH	$S_0 \rightarrow S_1$	H→L (67%)	423	2.93	1.148
	$S_0 \rightarrow S_2$	H-1→L (68%)	367	3.38	0.036
	$S_0 \rightarrow S_3$	H→L+1 (58%)	336	3.68	0.334
DPO-OPV3-Th-COOH	$S_0 \rightarrow S_1$	H→L (67%)	434	2.86	1.221
	$S_0 \rightarrow S_2$	H-1→L (67%)	372	3.34	0.064
	$S_0 \rightarrow S_3$	H→L+1 (66%)	368	3.37	0.401

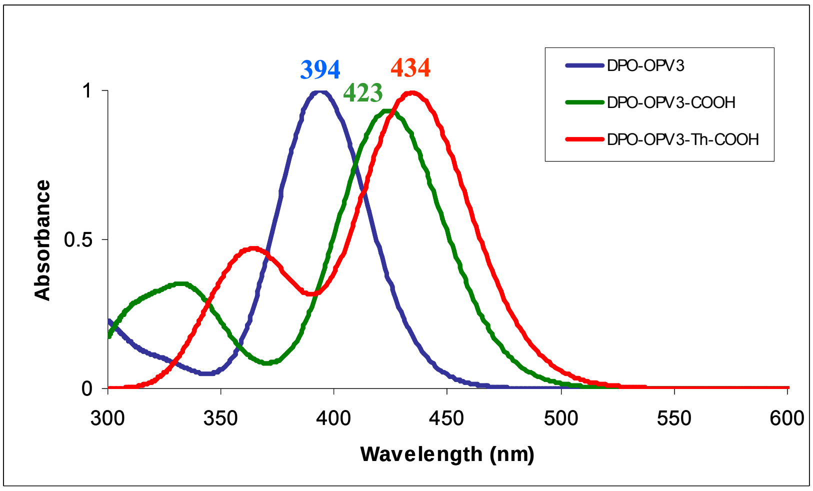

Figure 27 Comparison of simulated absorption spectra for DPO-OPV3, DPO-OPV3-COOH, and DPO-OPV3-Th-COOH using TD-B3LYP/6-31G* method with CPCM solvent to include the effect of toluene

The red-shift to the visible range of the absorption spectra due to the expansion of π-conjugated system in DPO-OPV3-Th-COOH, compared to DPO-OPV3 and DPO-OPV3-COOH, are desirable for gaining the sun light as photo-sensitizer in dye sensitized solar cells.

The HOMO and LUMO orbitals of all compounds are shown in Figure 28. The LUMO orbital possesses over all position of carboxyl group and the larger composition over the carboxyl connected to the thiophene spacer group. The results show that electron transfer from phenylenevinylene chromophore via thiophene spacer to carboxyl anchor group takes place during the excitation process of DPO-OPV3-Th COOH, but in the case of DPO-OPV3, electron delocalized in the phenylenevinylene ring cannot be transferred to the side of spacer and anchor groups of molecule.

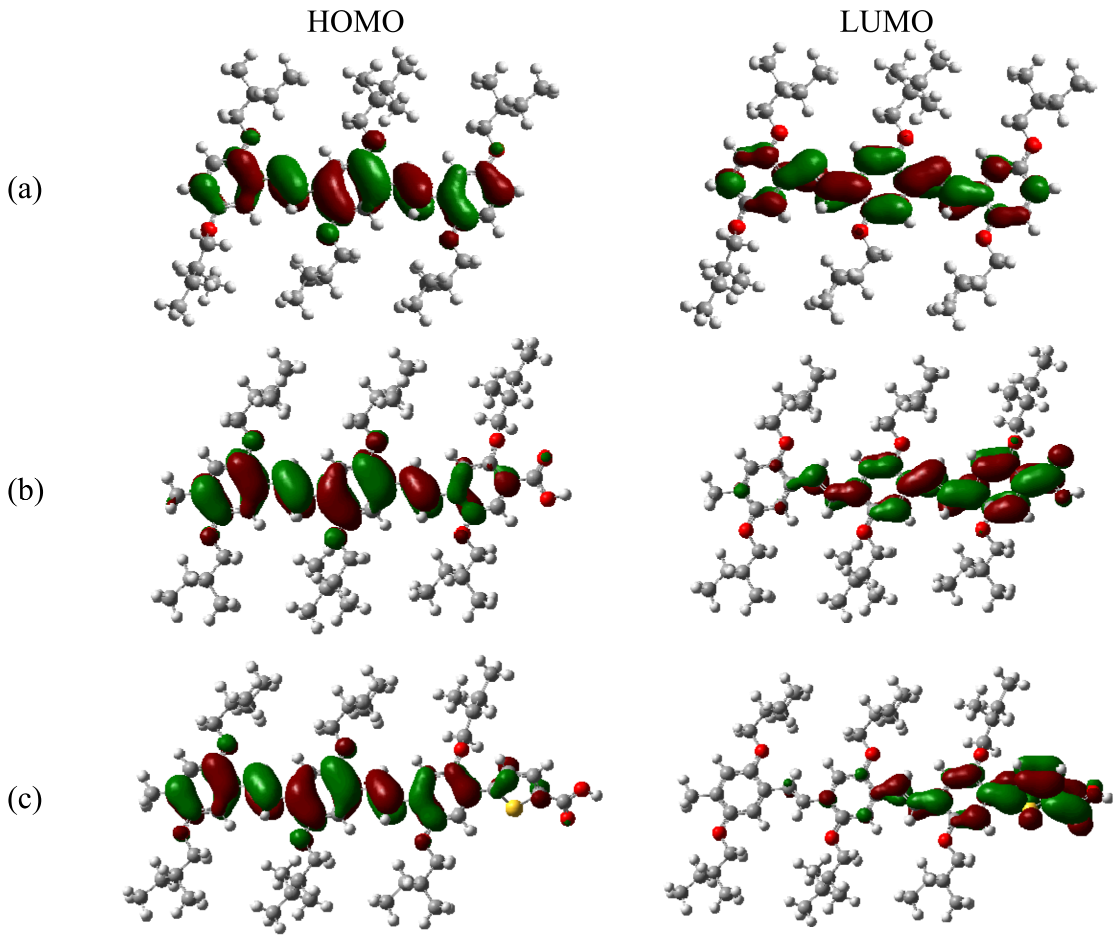

Figure 28 Calculated HOMO and LUMO orbitals for (a) DPO-OPV3, (b) DPO-OPV3-COOH, and (c) DPO-OPV3-Th-COOH

The percentages of electron distributions show the difference on the density of molecular orbitals between HOMO and LUMO of all compounds were calculated to explain the electron transfer from the ground state to the excited state. These results are shown in Table 7

Table 7 Percentage of electron distribution of HOMO and LUMO for DPO-OPV3, DPO-OPV3-COOH, and DPO-OPV3-Th-COOH

Compound	Excitation	% Distribution			
		Side chain	Chromophore	Anchor	Spacer
DPO-OPV3					
	LUMO	1	99	-	-
	HOMO	3	97	-	-
	% transfer	-2	2	-	-
DPO-OPV3-COOH					
	LUMO	1	88	11	-
	HOMO	3	97	0	-
	% transfer	-2	-9	11	-
DPO-OPV3-Th-COOH					
	LUMO	1	51	12	36
	HOMO	3	96	0	1
	% transfer	-2	-45	12	35

The difference of the distribution between HOMO and LUMO for DPO-OPV3 is very small (2%), compared with that of DPO-OPV3-COOH (11%), which was decreased to 2% at side chain, 9% at chromophore, but increased to 11% at anchor group. The distribution in DPO-OPV3-Th-COOH is 47% that was decreased to 2% at side chain and 9% at chromophore, but increased to 12% at anchor group and 35% at spacer group. The results indicate that the electron of chromophore is transferred to anchor during excitation from HOMO to LUMO in the case of DPO-OPV3-COOH whereas it is delocalized via spacer towards anchor in DPO-OPV3-Th-COOH.

In order to proceed of the electron injection to the conduction band of TiO_2, the electron was transferred from the chromophore to the carboxyl group which anchor with the surface of the semiconductor. Moreover, the spacer that links between the chromophore and the acceptor, such as thiophene, can increase the magnitude of the electron transfer in DPO-OPV3-Th-COOH

4. Effect of side chain

Various alkoxy substituents of DPO-OPV3-COOH with the thiophene spacer, OPV3-Th-COOH, DMO-OPV3-Th-COOH, and DPO-OPV3-Th-COOH were selected to investigate the chain-length dependence of the geometrical structures and electronic properties of the oligomer derivatives. The ground state geometries, obtained with HF/6-31G* optimization, are shown in Figure 29.

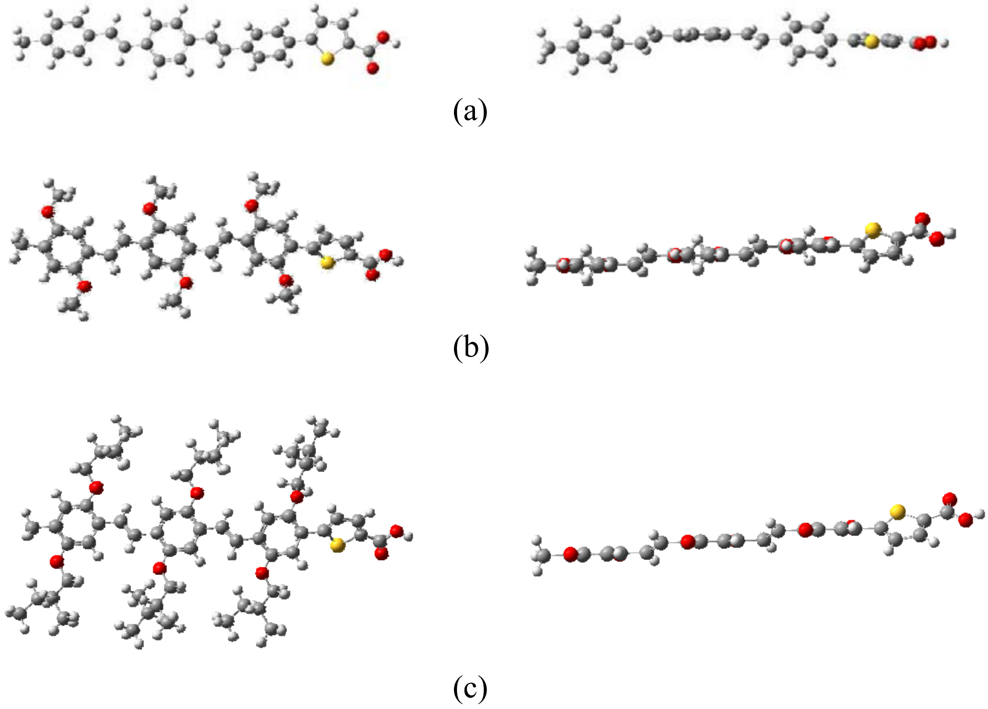

(a)

(b)

(c)

Figure 29 Top and side view of optimized structures (a) OPV3-Th-COOH, (b) DMO-OPV3-Th-COOH, and (c) DPO-OPV3-Th-COOH

From the side view of structures, the phenylenevinylene rings of DMO-OPV3-Th-COOH (Figure 29(b)) and DPO-OPV3-Th-COOH (Figure 29(c)) are in the coplanar conformation, but that of OPV3-Th-COOH (Figure 29(a)) prefers out-of-plane conformation in which the disorderly twist was found around vinylene linkages.

It demonstrates the interaction between oxygen atom of the alkoxy side chain and hydrogen atom at vinylene linkage leads to the coplanar conformation. The chain-length of alkoxy group on side chain does not affect the molecule configuration.

The electronic transition and the simulated absorption spectra of all compounds are presented in Table 8 and Figure 30, respectively. The most probable transition of all compounds is corresponded to the excitation from HOMO to LUMO. The maximum absorption wavelength of OPV3-Th-COOH, DMO-OPV3-Th-COOH, and DPO-OPV3-Th-COOH are 395, 433, and 434 nm, respectively. The wavelength of the twisted conformation of OPV3-Th-COOH that π-conjugate is smaller shifted to the longer wavelength with the size expansion for DMO-OPV3-Th-COOH and DPO-OPV3-Th-COOH in the coplanar configuration.

The absorption spectra of DMO-OPV3-Th-COOH and DPO-OPV3-Th-COOH are the same. It indicates that the length of alkoxy group does not be effect to the conformation structure and the excitation energy of the molecule.

Table 8 Calculated electronic transitions for OPV3-Th-COOH, DMO-OPV3-Th-COOH, and DPO-OPV3-Th-COOH using TD-B3LYP/6-31G*//HF/6-31G* method

Compound	State	Excitation	λ		*f*
			nm	eV	
OPV3-Th-COOH	$S_0 \rightarrow S_1$	H→L (67%)	395	3.14	2.032
	$S_0 \rightarrow S_2$	H+1→L (68%)	332	3.74	0.382
	$S_0 \rightarrow S_3$	H→L+1 (58%)	320	3.88	0.063
DMO-OPV3-Th-COOH	$S_0 \rightarrow S_1$	H→L (67%)	433	2.86	1.289
	$S_0 \rightarrow S_2$	H+1→L (67%)	370	3.35	0.093
	$S_0 \rightarrow S_3$	H→L+1 (67%)	363	3.41	0.397
DPO-OPV3-Th-COOH	$S_0 \rightarrow S_1$	H→L (67%)	434	2.86	1.221
	$S_0 \rightarrow S_2$	H+1→L (67%)	372	3.34	0.064
	$S_0 \rightarrow S_3$	H→L+1 (66%)	368	3.37	0.401

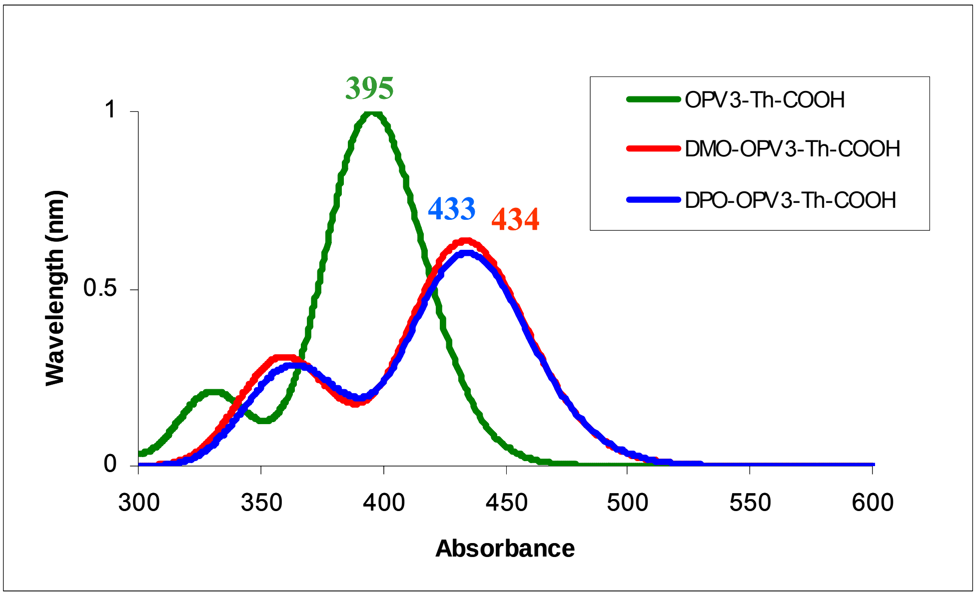

Figure 30 Comparison of simulated absorption spectra for OPV3-Th-COOH, DMO-OPV3-Th-COOH, and DPO-OPV3-Th-COOH using TDB3LYP/6-31G* method with CPCM to include the solvent effect of toluene

The structures of HOMO-LOMO (Figure 31) and the percentage of electron distribution (Table 9) of these compounds indicate that electron will transfer from phenylene chromophore via thiophene spacer to carboxyl anchor group during the excitation from HOMO (ground state) to LUMO (excited state). The difference of percent distribution between HOMO and LUMO at chromophore of DMO-OPV3-Th-COOH (-45%) and DPO-OPV3-Th-COOH (-45%) are the same, but more than that of OPV3-Th-COOH (27%). It demonstrates that the higher π-conjugated system of DMO-OPV3-Th-COOH and DPO-OPV3-Th-COOH (coplanar structure) transfer the electron from chromophore to anchor more than the lower that of OPV3-Th-COOH (twisted conformation)

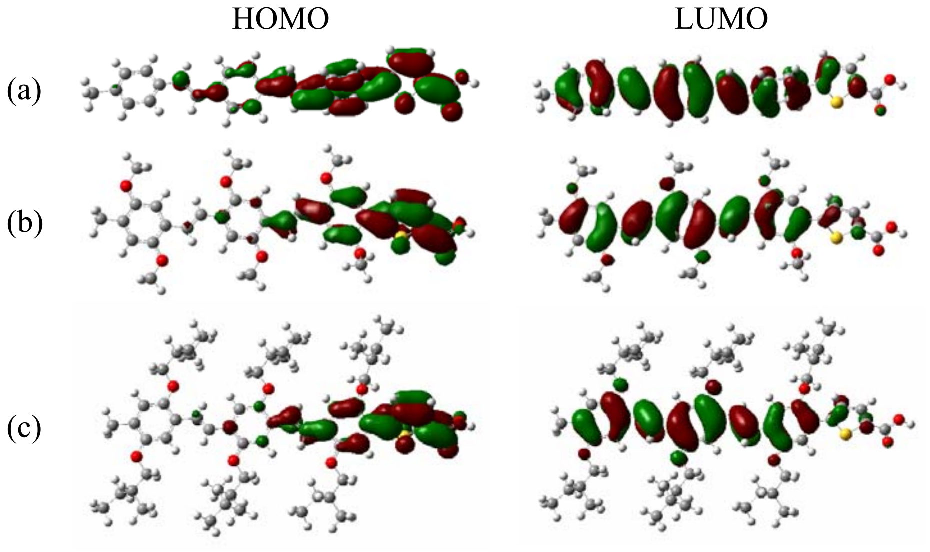

Figure 31 Calculated HOMO and LUMO orbitals for (a) OPV3-Th-COOH, (b) DMO OPV3-Th-COOH, and (c) DPO-OPV3-Th-COOH

Table 9 Percentage of electron distribution of HOMO and LUMO for OPV3-Th-COOH, DMO-OPV3-Th-COOH, and DPO-OPV3-Th-COOH

Compound	State	% Distribution			
		Side chain	Chromophore	Anchor	Spacer
OPV3-Th-COOH					
	LUMO	-	69	7	24
	HOMO	-	96	0	4
	% transfer	-	-27	7	20
DMO-OPV3-Th-COOH					
	LUMO	1	51	12	36
	HOMO	3	96	0	1
	% transfer	-2	-45	12	35
DPO-OPV3-Th-COOH					
	LUMO	1	51	12	36
	HOMO	3	96	0	1
	% transfer	-2	-45	12	35

Consequently, the alkoxy side chains cause the coplanarization in DMO-OPV3-Th-COOH and DPO-OPV3-Th-COOH compounds that lead to the expansion of π-conjugated system, the red-shift of absorption band, and the electron transfer enhancement. The chain-length has no effect on the structure and electronic properties of this molecule.

5. Spacer modeling

In this part, DMO-OPV3-COOH was selected to be introduced with various thiophene spacer groups as Thiophene, Di-thiophene, Vinylene-thiphene, Thiophene-vinylene-thiophene, and Di-vinylene-thiphene (Figure 32). These spacer groups are used for the sensitizers that are expected to possess a broad spectrum in the visible light region, an intense absorption, and the electron transfer enhancement to the semiconductor. The ground state geometries were optimized and electronic transitions were calculated using HF/6-31G* and TD-B3LYP/6-31G* methods, respectively.

The geometry optimization results show that the conformation of chromophore in all compounds is coplanar, but the spacer linkage was twisted out of the plane of the chromophore. The torsion angle between the chromophore and the thiophene linkage in DMO-OPV3-Th-COOH, DMO-OPV3-di-Th-COOH, and DMO-OPV3-Th-Vi-Th-COOH (38°) is more twisted than that of vinylene linkage in DMO-OPV3-Vi-Th-COOH and DMO-OPV3-di-Vi-Th-COOH (25°).

Excitation energies and oscillator strength for the transition from ground state (S_0), to first (S_1), second (S_2), and third singlet excited state (S_3) of all compounds are listed in Table 10. The oscillator strength of the $S_0 \rightarrow S_1$ is the highest of all transitions, corresponding excitation from HOMO to LUMO.

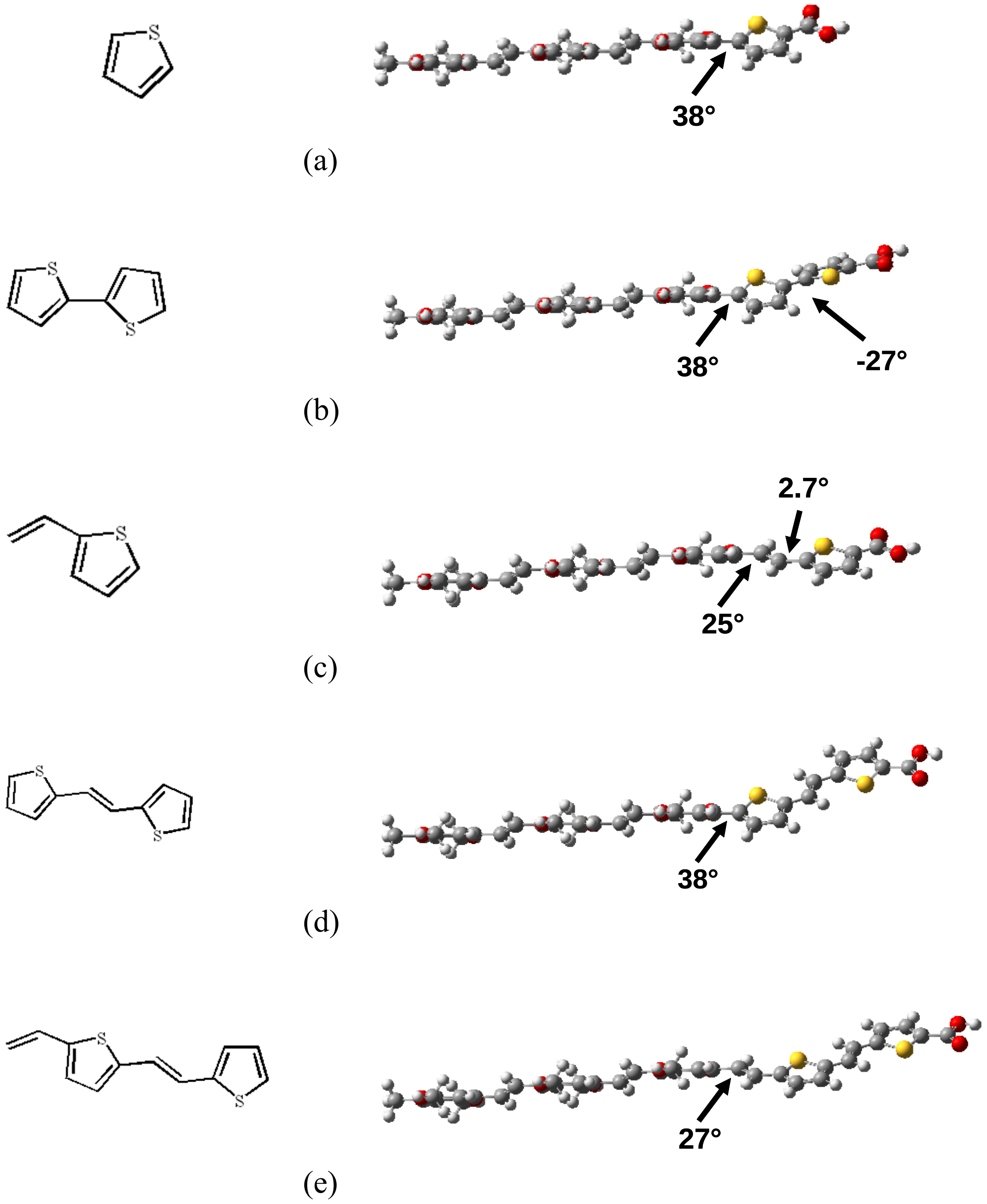

Figure 32 Chemical structures of spacers and side view of the optimized structure of (a) DMO-OPV3-Th-COOH, (b) DMO-OPV3-di-Th-COOH, (c) DMO-OPV3-Vi-Th-COOH, (d) DMO-OPV3-Th-Vi-Th-COOH, and DMO-OPV3-di-Vi-Th-COOH

Table 10 Calculated electronic transitions for DMO-OPV3-Th-COOH, DMO-OPV3-di-Th-COOH, DMO-OPV3-Vi-Th-COOH, DMO-OPV3-Th-Vi-Th-COOH, and DMO-OPV3-di-Vi-Th-COOH using TD-B3LYP/6-31G*//HF/6-31G* method

Compound	State	Excitation	λ_{cal}		*f*
			nm	eV	
DMO-OPV3-Th-COOH	$S_0 \rightarrow S_1$	H→L (67%)	433	2.86	1.289
	$S_0 \rightarrow S_2$	H-1→L (67%)	370	3.35	0.093
	$S_0 \rightarrow S_3$	H→L+1 (67%)	363	3.41	0.397
DMO-OPV3-di-Th-COOH	$S_0 \rightarrow S_1$	H→L (66%)	444	2.79	1.295
	$S_0 \rightarrow S_2$	H→L+1 (62%)	387	3.20	0.771
	$S_0 \rightarrow S_3$	H-1→L (66%)	381	3.26	0.138
DMO-OPV3-Vi-Th-COOH	$S_0 \rightarrow S_1$	H→L (67%)	468	2.65	1.213
	$S_0 \rightarrow S_2$	H-1→L (64%)	397	3.13	0.455
	$S_0 \rightarrow S_3$	H→L+1(66%)	381	3.26	0.666
DMO-OPV3-Th-Vi-Th-COOH	$S_0 \rightarrow S_1$	H→L (66%)	469	2.64	1.176
	$S_0 \rightarrow S_2$	H-1→L (57%)	410	3.02	1.002
	$S_0 \rightarrow S_3$	H→L+1 (62%)	397	3.12	0.465
DMO-OPV3-di-Vi-Th-COOH	$S_0 \rightarrow S_1$	H→L (66%)	501	2.47	1.425
	$S_0 \rightarrow S_2$	H-1→L (62%)	438	2.83	0.781
	$S_0 \rightarrow S_3$	H-2→L (64%)	406	3.05	0.730

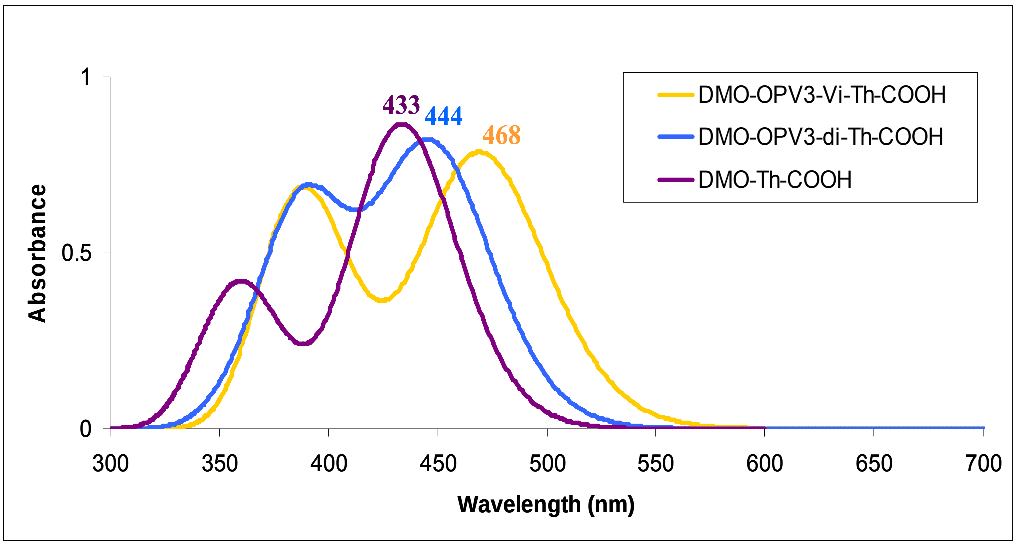

(a)

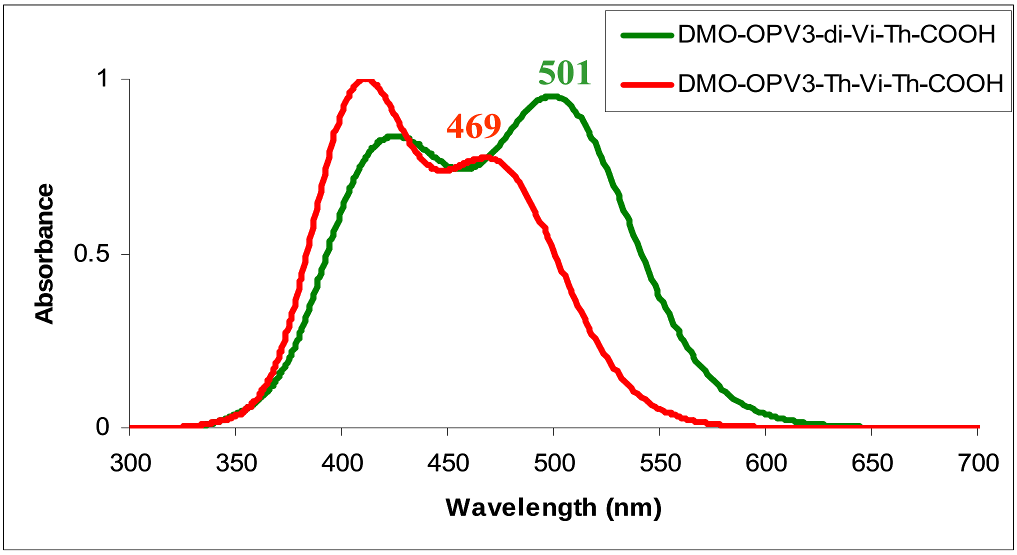

(b)

Figure 33 Comparison of simulated absorption spectra for (a) DMO-OPV3-Th-COOH, DMO-OPV3-di-Th-COOH, and DPO-OPV3-Vi-Th-COOH and (b) DMO-OPV3-Th-Vi-Th-COOH and DMO-OPV3-di-Vi-Th-COOH using TD-B3LYP/6-31G* method with CPCM to include the solvent effect of toluene

The calculated spectra of all compounds are presented in Figure 33. The maximum absorption wavelength of these compounds is labeled in Figure 33. It shows that the size expansion of π-conjugation for the longer spacers causes the red-shift and the broad band in the visible light region.

For the comparison of two spacers, the absorption wavelength of DMO-OPV3-Vi-Th-COOH (468 nm) is longer than that of DMO-OPV3-di-Th-COOH (444 nm) because of the planarization of the structure as shown in Figure 32. The conformation between the chromophore and the spacer of DMO-OPV3-Vi-Th-COOH is more planar than DMO-OPV3-di-Th-COOH. The spacer cause higher π-conjugated system in the structure. For longer spacer, the wavelength of DMO-OPV3-di-Vi-Th-COOH is longer than that of DMO-OPV3-Th-Vi-Th-COOH, which can be explained with the same reason with the case of two function spacers. Then, the vinylene linkage spacer leads to the planar conformation, which causes the high π-conjugatation, and the broad absorption in visible region compared with the thiophene linkage.

Although the maximum absorption wavelength of the vinylene linkage is longer than that of thiophene linkage, the percentages of the electron transfer in DMO-OPV3-di-Th-COOH (75%) and DMO-OPV3-Th-Vi-Th-COOH (82%) are more than DMO-OPV3-Vi-Th-COOH (65%) and DMO-OPV3-di-Vi-Th-COOH (77%). It indicates that the thiophene linkage spacer increases the efficiency of electron transfer from the chromophore to the anchor better than the vinylene linkage. However, the limit of the carboxyl group as the electron acceptor from the chromophore and the spacer is about 10-13%. So, the anchor group should be modeled with other acceptor to improve the efficiency of the electron transfer.

Table 11 Percentage of electron distribution of HOMO and LUMO for DMO-OPV3-Th-COOH, DMO-OPV3-di-Th-COOH, DPO-OPV3-Vi-Th-COOH, DMO-OPV3-Th-Vi-Th-COOH, and DMO-OPV3-di-Vi-Th-COOH

Compound	State	% Distribution			
		Side chain	Chromophore	Anchor	Spacer
DMO-Th-COOH					
	LUMO	1	51	11	29
	HOMO	3	96	0	1
	% transfer	-2	-45	11	28
DMO-di-Th-COOH					
	LUMO	0	19	13	68
	HOMO	3	94	0	3
	% transfer	-3	-75	13	65
DMO-Vi-Th-COOH					
	LUMO	1	29	11	59
	HOMO	3	94	0	3
	% transfer	-2	-65	11	56
DMO-Th-Vi-Th-COOH					
	LUMO	0	11	10	79
	HOMO	3	93	0	4
	% transfer	-3	-82	10	75
DMO-di-Vi-Th-COOH					
	LUMO	0	10	8	82
	HOMO	5	87	0	8
	% transfer	-5	-77	8	74

6. Anchor modeling

Acrylic group (Figure 8(b)) that strong electron withdrawing is anchor to model the new compound, comparison with carboxyl group as shown the optimized structures in Figure 34.

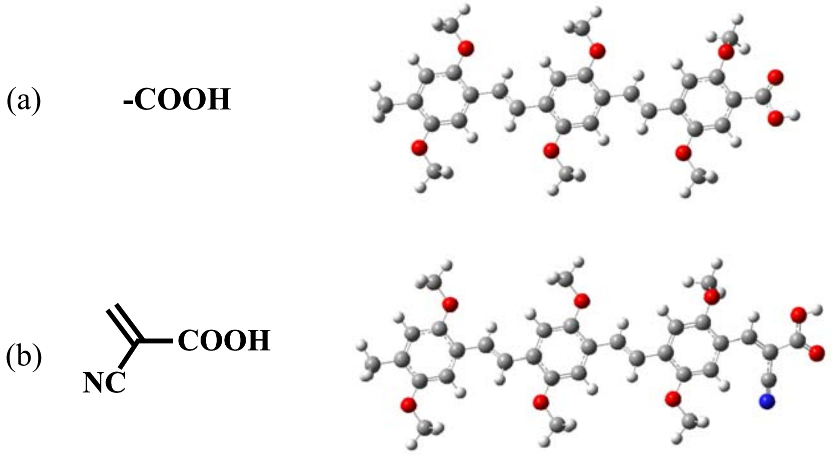

Figure 34 Chemical structures of (a) DMO-OPV3-COOH and (b) DMO-OPV3-CN-COOH

Calculated electronic transitions from TD-B3LYP/6-31G* method (Table 12) indicate that the most probable transition for the DMO-OPV3-COOH is the S_0→S_1 (HOMO→LUMO) transition, whereas DMO-OPV3-CN-COOH has two dominant transitions, which are the S_0→S_1 (0.724) and the S_0→S_2 (0.596), corresponding HOMO→LUMO and HOMO→LUMO+1 transitions, respectively. Simulated absorption spectra of these compounds in Figure 35 show one absorption region of DMO-OPV3-COOH which is related to the excitation from HOMO to LUMO at the maximum wavelength of 422 nm. The two absorption regions of DMO-PV3-CN-COOH are the HOMO→LUMO and the HOMO→LUMO+1 at 530 and 380 nm, respectively. The broad absorption in longer wavelength indicates that DMO-OPV3-CN-COOH is a potential sensitizer for DSSCs.

Table 12 Calculated electronic transitions for DMO-OPV3-COOH and DMO-OPV3-CN-COOH using TDb3LYP/6-31G*//HF/6-31G* method

Compound	State	Excitation	λ_{cal}		f
			nm	eV	
DMO-OPV3-COOH	$S_0 \rightarrow S_1$	H→L (67%)	422	2.94	1.191
	$S_0 \rightarrow S_2$	H-1→L (67%)	365	3.40	0.031
	$S_0 \rightarrow S_3$	H→L+1 (66%)	336	3.69	0.365
DMO-OPV3-CN-COOH	$S_0 \rightarrow S_1$	H→L (67%)	533	2.33	0.724
	$S_0 \rightarrow S_2$	H-1→L (67%)	446	2.78	0.118
	$S_0 \rightarrow S_3$	H→L+1 (66%)	397	3.12	0.596

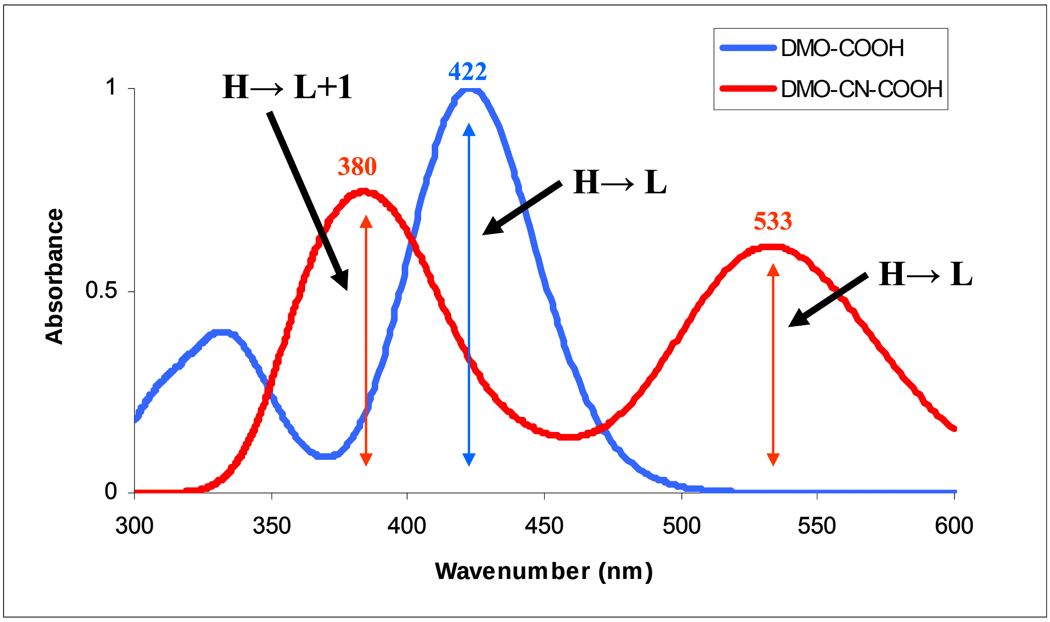

Figure 35 Comparison of simulated absorption spectra for DMO-OPV3-COOH and DMO-OPV3-CN-COOH using TD-B3LYP/6-31G* method with CPCM to include the solvent effect of toluene

The shape of molecular orbitals (Figure 36) and the percentage of electron distribution ns (Table 13) demonstrate that the electron transfer efficiency of DMO-OPV3-CN-COOH due to the acrylic group is increased to 53%, from 11% due to the carboxyl group in DMO-OPV3-COOH. The electron injection process from acrylic anchor group to semiconductor conduction band is therefore expected to be more efficiency than that of carboxyl group.

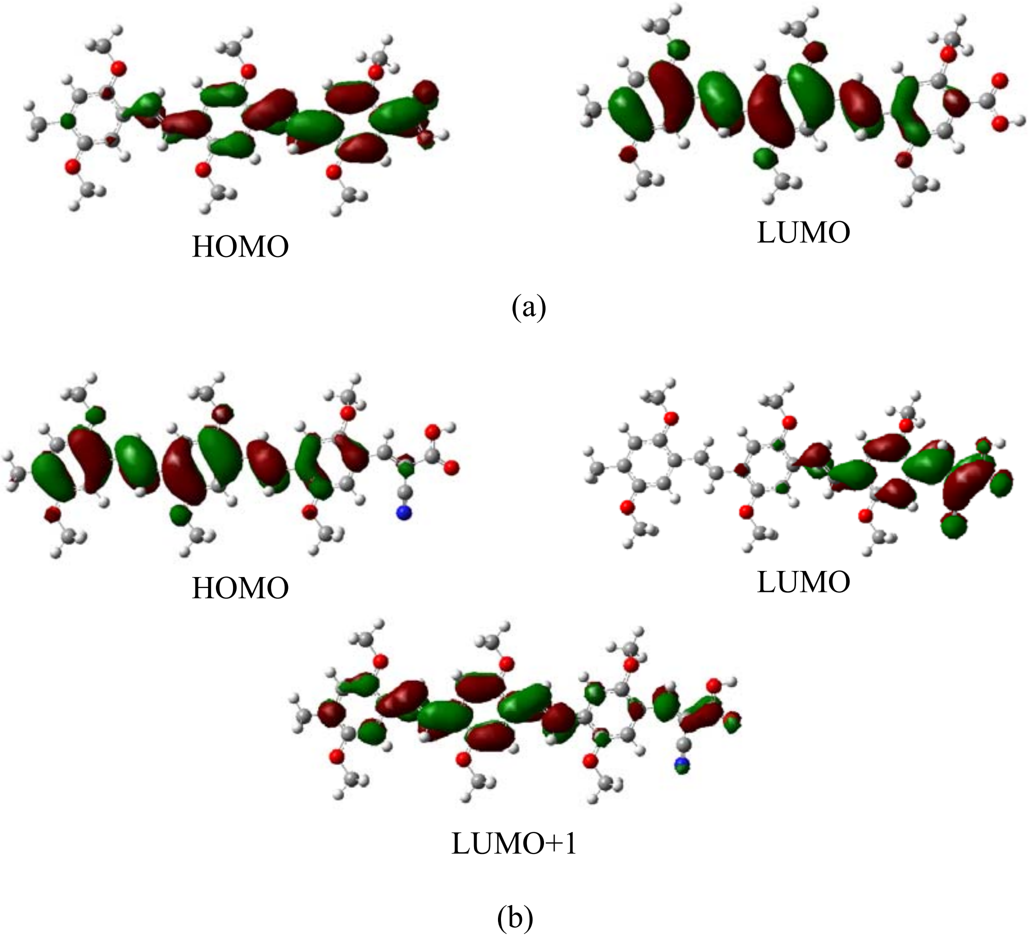

Figure 36 Calculated molecular orbital structures for (a) DMO-OPV3-COOH and (b) DMO-OPV3-CN-COOH

Table 13 Percentage of electron distribution of HOMO and LUMO for DMO-OPV3-COOH and HOMO, LUMO, and LUMO+1 for DMO-OPV3-CN-COOH

Compound	State	% Distribution		
		Side chain	Chromophore	Anchor
DMO-OPV3-COOH				
	LUMO	1	88	11
	HOMO	3	97	0
	% transfer	-2	-9	11
DMO-OPV3-CN-COOH				
	LUMO+1	1	87	12
	LUMO	1	45	54
	HOMO	3	96	1
	% transfer H→L	-2	-51	53
	% transfer H→L+1	-2	-9	11

CONCLUSION

Structures and IR frequencies of DPO-OPV3-COOH and its derivatives geometries using HF, B3LYP and MP2 methods with 6-31G* basis set are in an agreement with the experimental data. The results show that these structures contains a weak intramolecular hydrogen bonding between oxygem atom of substituted alkoxy group onto the phenylene ring at the ortho-carbon and hydrogen atom on the vinylene linkage leading to the planarization of the phenylenevinylene chromophore.

To confirm the optimized geometry, the structures of DPO-OPV3-COOH from various methods were calculated the electronic properties using TD-B3LYP/6-31G* method with CPCM to include the toluene solvation effect and compared with the experimental absorption band of this molecule in toluene solvent. The excitation result of the coplanar structure obtained from HF/6-31G* method is closer to the experimental data than that of the planar structure obtained from B3LYP/6-31G* method. The MP2/6-31G* calculations is used to confirm the accuracy of the HF/6-31G* method. Therefore, in this study, TD-B3LYP/ 6-31G*//HF/6-31G* method and the coplanar ground state geometry of phenylenevinylene chromophore were selected to investigate the effects of spacer and anchor groups for the structures and electronic properties of DPO-OPV3-COOH derivatives.

The molecular orbitals and HOMO-LUMO energy values for DPO-OPV3-COOH demonstrate that electron will be transferred from the phenylenevinylene chromophore toward the carboxyl anchor group and inject to the conduction band of TiO_2 semiconductor during the excitation process. The excited state energy levels for this molecule are much higher than the bottom of the conduction band of TiO_2. It indicates that electron injection process is viable. We therefore propose DPO-OPV3-COOH as a potential sensitizer for DSSCs.

According to the anchor group such as carboxylic acid which anchors with the surface of semiconductor, the electron is transferred from the chromophore to the anchor group. The spacer group such as thiophene that links between chromophore and anchor group can increases the electron transfer and expand the π-conjugated system, thus the observation of the absorption band in the visible light region. The more electron transfer and the red-shift in the absorption band from DPO-OPV3, DPO-OPV3-COOH to DPO-OPV3-Th-COOH are desirable for gaining the sun light and good character as photo-sensitizer in DSSCs.

The methoxy side chain (-OCH_3), Di-vinylene-thiophene spacer (di-Vi-Th), and acrylic acid anchor (CN-COOH) can increase the electron transfer and the visible light absorption. Methoxy side chain causes coplanar configuration at the phenylenevinylene chromophore. Divinylenethiophene spacer lead to the expansion of π-conjugated system and bathochromically extended absorption spectra. Larger amount of electron can be introduced by acrylic acid anchor from the chromophore.

For the present study of the modeling of side chain, spacer, and anchor, the new sensitizer of DMO-OPV3-di-Vi-Th-CN-COOH (Figure 37), whose efficiencies of electron transfer and absorption are enhance, is therefore suggested for the further study and synthesis in the laboratory.

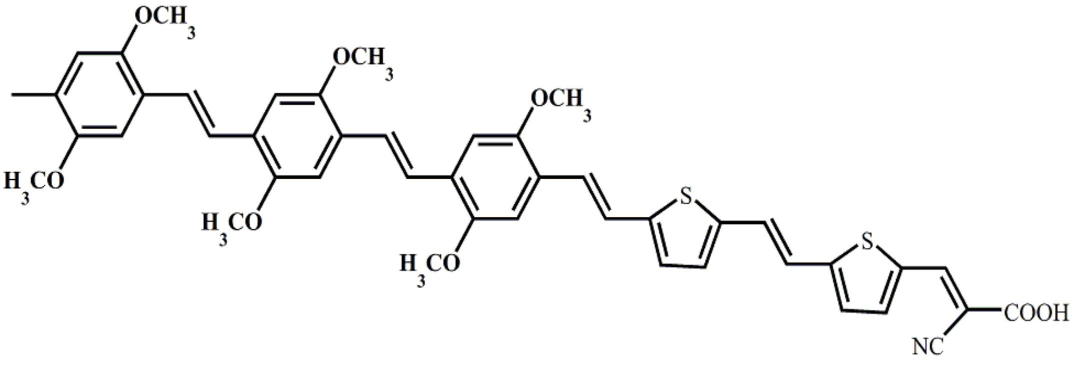

Figure 37 Chemical structure of the proposed sensitizer of DMO-OPV3-di-Vi-Th-CN-COOH

LITERATURE CITED

Alam, M. M. and S. A. Jenekhe. 2004. Efficient Solar Cells from Layered Nanostructures of Donor and Acceptor Conjugated Polymers. **Chem. Mater.** 16: 4647-4656.

Asbury, J. B., E. Hao, Y. Wang, H. N. Ghosh and T. Lian. 2001. Ultrafast Electron Transfer Dynamics from Molecular Adsorbates to Semiconductor Nanocrystalline Thin Films. **J. Phys. Chem. B.** 105(20): 4545-4557.

Campbell, W. M., K. W. Jolley, P. Wagner, P. J. Walsh, K. C. Gordon, L. Schmidt-Mende, M. K. Nazeeruddin, Q. Wang, M. Gra1tzel and D. L. Officer. 2007. Highly Efficient Porphyrin Sensitizers for Dye-Sensitized Solar Cells. **J. Phys. Chem. C.** 111: 11760-11762.

Chang, R., J. H. Hsu, W. S. Fann, K. K. Liang, C. H. Chang, M. Hayashi, J. Yu, S. H. Lin, E. C. Chang, K. R. Chuang and S. A. Chen. 2000. Experimental and Theoretical Investigations of Absorption and Emission Spectra of the Light-Emitting Polymer MEH-PPV in Solution. **Chemical Physics Letters**. 317: 142–152.

Chen, C. Y., S. J. Wu, C. G. Wu, J. G. Chen and K. C. Ho. 2006. A Ruthenium Complex with Superhigh Light-Harvesting Capacity for Dye-Sensitized Solar Cells. **Angew. Chem., Int. Ed.** 45: 5822.

Finder, W., F.Bogar and R.Knab. 1998. Energy bands and bond alternation potential in poly(1,4-phenylene vinylene): a comparative ab initio quantum chemical and density function theory study. **J. Mol. Struct. (THEOCHEM)** 430: 73-84.

Gratzel, M. and B. O'Reagen. 1991. A Low-Cost, High-Efficiency Solar Cell Based on Dye-Sensitized Colloidal TiO_2 Films. **Nature.** 353: 737-740.

Hagberg, D. P., K. M. Karlsson, T. Marinado, G. Boschloo, A. Hagfeldt and L. Sun. 2007. Tuning the HOMO and LUMO Energy Levels of Organic Chromophores for Dye Sensitized Solar Cells. **J. Org. Chem**. 72: 9550-9556.

Hagfeldt, A., J. He, H. Lindstrom and S. E. Lindquist. 2000. Dye-Sensitized Nanostructured Tandem Cell-First Demonstrated Cell with a Dye-Sensitized Photocathode. **Solar energy materials and solar cells**. 62: 265-273.

Hal, P. A., M. M. Wienk, J. M. Kroon and R. A. J. Janssen. 2003. TiO_2 Sensitized with an Oligo(p-phenylenevinylene) carboxylic acid: a New Model Compound for a Hybrid Solar Cell. **J. Mater. Chem**. 13: 1054-1057.

Labat, F., P. Baranek and C. Adamo. 2008. Structural and Electronic Properties of Selected Rutile and Anatase TiO_2 Surfaces: An ab Initio Investigation. **J. Chem. Theory. Comput**. 4: 341-352.

Lundqvist, M. J., M. Nilsing, S. Lunell, B. Akermark and P. Persson. 2006. Spacer and Anchor Effects on the Electronic Coupling in Ruthenium-bis-Terpyridine Dye-Sensitized TiO2 Nanocrystals Studied by DFT. **J. Phy. Chem. B**. 110: 20513-20525.

Mattsson, A., M. Leideborg, K. Larsson, G. Westin and L. Osterlund. 2006. Adsorption and Solar Light Decomposition of Acetone on Anatase TiO_2 and Niobium Doped TiO_2 Thin Films. **J. Phy. Chem. B**. 110: 1210-1220.

Matsuura, H., H. Yoshida, M. Heida, S. Yamanaka and T. Harada. 2003. Experimental Evidence for Intramolecular Blue-Shifting C-H...O hydrogen Bonding by Matrix-Isolation Infrared Spectroscopy **J. Am. Chem. Soc.** 125(46): 13910-13911.

Nazeeruddin, M. K., P. Pechy, T. Renouard, S. M. Zakeeruddin, P. Comte and M. Gratzel. 2001. Engineering of Efficient Panchromatic Sensitizers for Nanocrystalline TiO2-Based Solar Cells. **J. Am. Chem. Soc.** 123: 1613.

Nilsing, M., S. Lunell, P. Persson and L. Ojamae. 2007. Dye-Sensitization of the TiO_2 Rutile (110) Surface by Perylene Dyes: Quantum-Chemical Periodic B3LYP Computations. **J. Phy. Chem. C**. 111: 12116-12123.

Nilsing, M., S. Lunell, P. Persson and L. Ojamae. 2005. Phosphonic Acid Adsorption at the TiO_2 Anatase (101) Surface Investigated by Periodic Hybrid HF-DFT Computations. **Surface Science.** 582: 49-60.

Ning, Z., Q. Zhang, W. Wu, H. Pei, B. Lui and H. Tian. 2008. Starburst Triarylamine Based Dyes for Efficient Dye-Sensitized Solar Cells. **J. Org. Chem**. 73(10): 3791-3797.

O'Boyle, N. M. and J. G. Vos. 2005. GuassSum 1.0. Dublin City University Available at **http://gaussum .sourceforge.net.**

Petrella, A., M. Tamborra, P. D. Cozzoli, M. L. Curri, M. Striccoli, P. Cosma, G. M. Farinola, F. Babudri, F. Naso and A. Agotiano. 2004. TiO_2 Nanocrystals-MEH-PPV Composite Thin Flims as Photoactive Material. **Thin Solid Flims**. 451: 64-68.

Psudievsky, O. Y., G. M. Telbiz and V. K. Rossokhaty. 2006. Effect of solvent nature on liquid-phase self-asemmbly of MEH-PPV/MCM-41 guest-host composites. **J. Mater. Chem**. 16: 2485-2489.

Schnadt, J., P. A. Brühwiler, L. Patthey, J. M. O'Shea, S. Södergren and M. Odelius. 2002. Experimental Evidence for Sub-3-fs Charge Transfer from an Aromatic Adsorbate to a Semiconductor. **Nature.** 418: 620 – 623.

Stalmach, U., D. Schollmeyer and H. Meier. 1999. Single-crytal structures of model compound for poly(2,5-dialkoxy-1,4-phenylene vinylene). **Chem. Mater.** 11(8): 2103-2106.

Sun, D., J. Fang, G. Yu and F. Ma. 2007. Intramolecular hydrogen bonding and photoinduced intramolecular proton and electron transfer in 2-(2'-hydroxy phenyl)benzotiazole. **J. Mol. Struct. (THEOCHEM)** 806: 105-112

Suramitr, S., T. Kerdcharoen, T. Srikhirin and S. Hannongbua. 2005. Electronic Properties of Alkoxy Derivatives of Poly(*para*-phenylenevinylene), Investigated by Time-Dependent Density Functional Theory Calculations. **Synthetic Metals**. 155: 27–34.

Tsai, M. S., Y. C. Hsu, J. T. Lin, H. C. Chen and C. P Hsi. 2007. Organic Dyes Containing 1*H*-Phenanthro[9,10-*d*]imidazole Conjugation for Solar Cells. **J. Phys. Chem. C.** 111: 18785-18793.

Vittadini, A., A. Selloni, F. P. Rotzinger and M. Gratzel. 2000. Formic Acid Adsorption on Dry and Hydrate TiO_2 Anatase (101) Surfaces by DFT Calculations. **J. Phy. Chem. B**. 104: 1300-1306.

Wachsmann-Hogiu, S., L. A. Peteanu, J. A. Lui and D. J. Yaron. 2003. The Effect of Structural and Microenvironmental Disorder on the Electronic Properties of Poly[2-methoxy,5-(2'-ethyl-hexoxy)-1,4-phenylene vinylene] (MEH-PPV) and Relate**. J. Phy. Chem. B**. 107: 5133-5143.

Wu, C., S. Tretiak and V. Y. Chernyak. 2007. Excited State and Optical Response of a Donor-Acceptor Substituted Polyene: A TD-DFT Study. **Chemical Physics Letters**. 433: 305-311.

Zhang, X., J. Zhang and Y. Xia. 2008. Molecular Design of Dyes with High Efficiency in Dye-sensitized Solar Cell. J. Photochem. Photobiol. A: Chem. 194: 167-172.

APPENDICES

Appendix A: Theoretical Background

The Theory of Quantum Chemical Calculations

Molecular orbital theory is concerned with predicting the properties of atomic and molecular systems. It is based upon the fundamental laws of quantum mechanics and uses a variety of mathematical transformation and approximation techniques to solve the fundamental equations, in contrast to semi-empirical models.

The Schrödinger Equation

The quantum chemical methods are based on finding solutions to the Schrödinger equation on molecular orbital theory. Quantum mechanics explains how entities like electrons have both particle-like and wave-like characteristics. The time independent Schrödinger equation for a molecule (n-electron and N-nuclei system):

$$H\psi(\vec{r},\vec{R}) = E\psi(\vec{r},\vec{R}) \qquad (1)$$

and the Hamiltonian is (in atomic units):

$$H = T + V$$

$$H = -\sum_{i=1}^{N}\frac{1}{2}\nabla_i^2 - \sum_{A=1}^{M}\frac{1}{2M_A}\nabla_A^2 - \sum_{i=1}^{N}\sum_{A=1}^{M}\frac{Z_A}{r_{iA}} + \sum_{i=1}^{N}\sum_{j>i}^{N}\frac{1}{r_{ij}} + \sum_{A=1}^{M}\sum_{B>A}^{M}\frac{Z_A Z_B}{R_{AB}} \qquad (2)$$

where T and V are the kinetic and potential energy operators, respectively, which separate out the motion of the nuclei from the motion of the electrons, equation (2) can be rewritten as

$$H = -\sum_{A=1}^{M}\frac{1}{2M_A}\nabla_A^2 + H_{el} \qquad (3)$$

This focus on the electronic Hamiltonian, H_{el}, and try to solve the electronic Schrödinger equation in the field of the fixed nuclei. The nuclear-nuclear repulsion term (the final in equation (2)) appears as a constant in H_{el}. Further assume the wave function $\psi(\vec{r},\vec{R})$ to be a product of an electronic and a nuclear part:

$$\psi(\vec{r},\vec{R}) = \psi_{elec}(\vec{r},\vec{R})\psi_{nucl}(\vec{R}) \qquad (4)$$

The justification for this is that the electrons are much lighter than the nuclei. This is called the Born-Oppenheimer approximation. The parametric $\vec{R}$ dependence of ψ_{elec} arises since the electron distribution depends implicitly on the particular nuclear arrangement for the system under study. The nuclear wave function, ψ_{nucl}, describes the vibrational, rotational and translational motion of the nuclei. From (1), (3) and (4) can obtain;

$$H\psi(\vec{r},\vec{R}) = H\psi_{elec}(\vec{r},\vec{R})\psi_{nucl}(\vec{R}) = \left(-\sum_{A=1}^{M}\frac{1}{2M_A}\nabla_A^2 + H_{el}\right)\psi_{elec}(\vec{r},\vec{R})\psi_{nucl}(\vec{R})$$

$$= \left(-\sum_{A=1}^{M}\frac{1}{2M_A}\nabla_A^2 + E_{el}\right)\psi_{elec}(\vec{r},\vec{R})\psi_{nucl}(\vec{R}) = E\psi_{elec}(\vec{r},\vec{R})\psi_{nucl}(\vec{R}) = E\psi \qquad (5)$$

The electronic wavefunction $\psi_{elec}(\vec{r},\vec{R})$ can be divided out from both sides of equation (5), provided that terms in $\nabla^2\psi_{elec}(\vec{r},\vec{R})$ are small, i.e. the electronic wavefunction changes slowly upon small displacements of the nuclear positions. Thus, if we neglect the influence of the nuclear derivative on the electron wave function (ψ_{el}) (i.e. the nuclei move slowly compared with the electrons) which can separate equation (5) into two equations, an electronic part:

$$H_{el}\psi_{el}(\vec{r},\vec{R}) = E_{el}(\vec{R})\psi_{el}(\vec{r},\vec{R}) \qquad (6)$$

where

$$H_{el} = -\sum_{i=1}^{N}\frac{1}{2}\nabla_i^2 - \sum_{i=1}^{N}\sum_{A=1}^{M}\frac{Z_A}{r_{iA}} + \sum_{i=1}^{N}\sum_{j>i}^{N}\frac{1}{r_{ij}} + \sum_{A=1}^{M}\sum_{B>A}^{M}\frac{Z_A Z_B}{R_{AB}} \quad (7)$$

and a nuclear part:

$$H_{nucl}\psi_{nucl}(\vec{R}) = E\psi_{nucl}(\vec{R}) \quad (8)$$

where

$$H_{nucl} = -\sum_{A=1}^{M}\frac{1}{2M_A}\nabla_A^2 + E_{el}(\vec{R}) \quad (9)$$

Hartree Fock Theory

An exact solution to the Schrödinger equation is not possible for any but the most trivial molecular systems. However, a number of simplifying assumptions and procedures do make an approximate solution possible for a large range of molecules. To simplify the treatment further, the next step is to assume that the electrons are non-interacting. This implies that (apart from the constant nuclear-nuclear repulsion term) which can rewrite the total n-electron Hamiltonian as a sum of n one-electron Hamiltonians,

$$H_{el} = \sum_{i=1}^{N} h(i) \quad (10)$$

$$h(i) = \left(-\frac{1}{2}\nabla_i^2 - \sum_{A=1}^{M}\frac{Z_A}{r_{iA}}\right) \quad (11)$$

This is clearly an oversimplification, since have neglected the electron-electron repulsion term $\frac{1}{r_{ij}}$. Equation (10) defines the independent particle model. The one-electron Hamiltonians (equation (11)) are termed core-Hamiltonians, since the only interactions included are those between the electrons and the bare nuclei. Including an average interaction term in the $\{h(i)\}$, these become effective one-electron Hamiltonians. As a consequence of equation (10), the total wave function can be rewritten as a product of n single-particle wave functions,

$$\psi(\vec{r}) = \phi_1(\vec{r}_1)\phi_2(\vec{r}_2)...\phi_n(\vec{r}_n) \tag{12}$$

or, take the electron spin into account,

$$\psi = \chi_1(\vec{x}_1)\chi_2(\vec{x}_2)...\chi_n(\vec{x}_n) \tag{13}$$

The spin orbitals $\{\chi_i(\vec{x}_i)\}$ are the products of the spatial orbitals $\phi_i(\vec{r}_i)$ and the spin functions ($\alpha(\omega)$ and $\beta(\omega)$); $\vec{x}_i$ denotes both the space and spin coordinates of electron i. The total independent particle spin-orbital wave function (equation (13)) is called a Hartree-product. This is an eigenfunction of the n-electron model Hamiltonian defined in equation (10), and the corresponding eigenvalue is a sum of the single-particle spin-orbital energies,

$$E_{el} = \sum_{i=1}^{M} \varepsilon_i \tag{14}$$

A further requirement on the state wave function (13) is that it must be anti-symmetric with respect to the interchange of coordinate r (both space and spin) of any two electrons,

$$\left|\psi(\vec{x}_1, \vec{x}_{2,...,} \vec{x}_n)\right|^2 = \left|\psi(\vec{x}_2, \vec{x}_1, ..., \vec{x}_n)\right|^2 \tag{15}$$

$$\psi(\vec{x}_1, \vec{x}_2, ..., \vec{x}_n) = \pm\psi(\vec{x}_2, \vec{x}_1, ..., \vec{x}_n) \tag{16}$$

It is also possible to write equation (16) in terms of a $n \times n$ determinant, a Slater determinant, which has the same antisymmetric properties:

$$\psi = (n!)^{-1/2} \begin{vmatrix} \chi_1(\vec{x}_1) & \chi_2(\vec{x}_1) & \cdots & \chi_n(\vec{x}_1) \\ \chi_1(\vec{x}_2) & \chi_2(\vec{x}_2) & & \\ \cdots & & \cdots & \\ \chi_1(\vec{x}_n) & \chi_2(\vec{x}_n) & \cdots & \chi_n(\vec{x}_n) \end{vmatrix} \qquad (17)$$

Which commonly is written like:

$$|\psi\rangle = (n!)^{-1/2} |\chi_1(\vec{x}_1), \chi_2(\vec{x}_2), \ldots, \chi_n(\vec{x}_n)\rangle \qquad (18)$$

It can easily be verified that the Slater determinant obeys the Pauli principle, as the determinant then becomes zero. The pre-factor $(n!)^{-1/2}$ is a normalisation constant, and the $\{\chi_i\}$ are assumed orthonormal. By antisym-metrizing the Hartree-product (13) in the form of a Slater determinant (17), that the probability of finding any two electrons at the same point in space (i.e. $\vec{x}_1 = \vec{x}_2$) is zero.

Through the wave functions, the effective potential is generated. This potential allows to refine wave functions, from which a new potential is obtained. The procedure is repeated until a stable, self-consistent solution is reached. Due to the iterative procedure, the initial guess of the wave function, can of course be chosen ad hoc. However, the better the initial guess is, the easier it is to reach a stable solution to the eigenvalue problems in a relatively short computational time, is provided by the variation principle. This can be stated in the following way: Given any approximate wave function, satisfying the correct boundary conditions, the expectation value of the energy obtained by this wave function never lies below the exact energy of the ground state. Expressed in mathematical terms:

$$E_e = \frac{\langle\psi|H_e|\psi\rangle}{\langle\psi|\psi\rangle} \geq E_{exact} \qquad (19)$$

A conceptually appealing model for the (trial) wave function of our molecular system, is to regard it as being constructed from molecular orbitals (MO). This description in analogous to the model used for the atomic orbitals (AO). The MO's, the elements of the wave function determinant, are in turn thought of as being constructed by a Linear Combination of Atomic Orbitals (LCAO).

$$\psi_i^{MO} = \sum_{\mu} c_{\mu i}\phi_{\mu}^{AO} \qquad (20)$$

The variational principle leads to following equations describing the molecular orbital expansion coefficients, c_{vi}, derived by Roothaan and by Hall:

$$\sum_{v=1}^{N}\left(F_{\mu v} - \varepsilon_i S_{\mu v}\right)c_{vi} = 0 \quad \mu = 1,2,..., N \qquad (21)$$

Equation 21 can be rewritten in matrix form:

$$FC = SC\varepsilon \qquad (22)$$

with

$$F_{\mu v} = H_{\mu v}^{core} + \sum_{\lambda\sigma} P_{\lambda\sigma}\left[\left(\mu v|\lambda\sigma\right) - \frac{1}{2}\left(\mu\lambda|v\sigma\right)\right] \qquad (23)$$

$$F_{\mu v} = H_{\mu v}^{core} + G_{\mu v} \qquad (24)$$

where $H_{\mu v}^{core}$, core-Hamiltonian matrix, defined as

$$H_{\mu\nu}^{\text{core}} = \int dr_1 \phi_\mu^*(1) h(1) \phi_\nu(1) \qquad (25)$$

The matrix P is the density matrix or charge- and bond-order matrix,

$$P_{\mu\nu} = 2\sum_{a}^{N/2} C_{\mu a} C_{\nu a}^* \qquad (26)$$

The matrix S is the overlap matrix, indicating the overlap between orbitals.

$$S_{\mu\nu} = \int dr_1 \phi_\mu^*(1) \phi_\nu(1) \qquad (27)$$

The term $(\mu\nu|\lambda\sigma)$ in Equation 23 signified the two-electron repulsion integrals, defined as

$$(\mu\nu|\lambda\sigma) = \int dr_1 dr_2 \phi_\mu^*(1) \phi_\nu(2) r_{12}^{-1} \phi_\lambda^*(2) \phi_\sigma(2) \qquad (28)$$

The (initial) wave function is used to generate an effective potential, which apply this potential in order to refine the coefficient matrix. The modified MO's form the new input in the Roothaan or Pople-Nesbet (1986) equations, and a new potential is generated. The iterative procedure is repeated until convergence is reached, i.e. when the changes in energy and/or charge density in two subsequent iterations are below a pre-set threshold value.

Before a more technical description of the SCF-procedure is presented, first need to define a new transformation matrix X, used for orthogonalisation of the basis set. This orthogonalisation can be either symmetric or canonical. A symmetric orthogonalisation implies that X is formed through the relation

$$X = S^{-1/2} = Us^{-1/2}U^{\tau} \qquad (29)$$

where S is the overlap matrix, U is an unitary matrix which diagonalizes S, and the diagonal matrix of the eigenvalues of S is given by the relations. In the canonical orthogonalisation procedure, X is instead given by

$$X = Us^{-1/2} \tag{30}$$

Consider a new coefficient matrix C' related to the old coefficient matrix C by

$$C' = X^{-1}C, \qquad C = XC' \tag{31}$$

where assumed that X possesses an inverse. Substituting $C = XC'$ into the Roothaan equations gives

$$FXC' = SXC'\varepsilon \tag{32}$$

Multiplying on the left by X^{τ} gives

$$\left(X^{\tau}FX\right)C' = \left(X^{\tau}SX\right)C'\varepsilon \tag{33}$$

if define a new matrix F^{τ} by

$$F^{\tau} = X^{\tau}FX \tag{34}$$

and use (27),then

$$F'C' = C'\varepsilon \tag{35}$$

The SCF procedure, outlined in Appendix figure I , is as follows

1. Specify a molecule (a set of nuclear coordinates $\{R_A\}$, atomic numbers $\{Z_A\}$, and number of electron N) and a basis set $\{\phi_\mu\}$.
2. Calculate all required molecular integrals, $S_{\mu\nu}$, $H^{core}_{\mu\nu}$ and $(\mu\nu|\lambda\sigma)$.
3. Diagonalize the overlap matrix S and obtain a transformation matrix X from either equation $X \equiv S^{-1/2} = Us^{-1/2}U^{\tau}$ or $X = Us^{-1/2}$.
4. Obtain a guess at the density matrix P.
5. Calculate the matrix G of equation $F_{\mu\nu} = H^{core}_{\mu\nu} + G_{\mu\nu}$ from the density matrix P and the two-electron integral $(\mu\nu|\lambda\sigma)$.
6. Add G to the core-Hamiltonian to obtain the Fock matrix $F = H^{core} + G$.
7. Calculate the transformed Fork matrix $F^{\tau} = X^{\tau}FX$
8. Diagonalize F^{τ} to obtain C' and ε.
9. Calculate $C = XC'$.
10. Form a new density matrix P from C using $P_{\mu\nu} = 2\sum_{a}^{N/2} C_{\mu a}C^{*}_{\nu a}$.
11. Determine whether the procedure has converged, i.e. determine whether the new density matrix of step (10) is the same as the previous density matrix within a specified criterion. If the procedure has not converged, return to step (5) with the new density matrix.
12. If the procedure has converged, then use the resultant solution, represented by C, P, F, etc., to calculate expectation values and other quantities of interest.

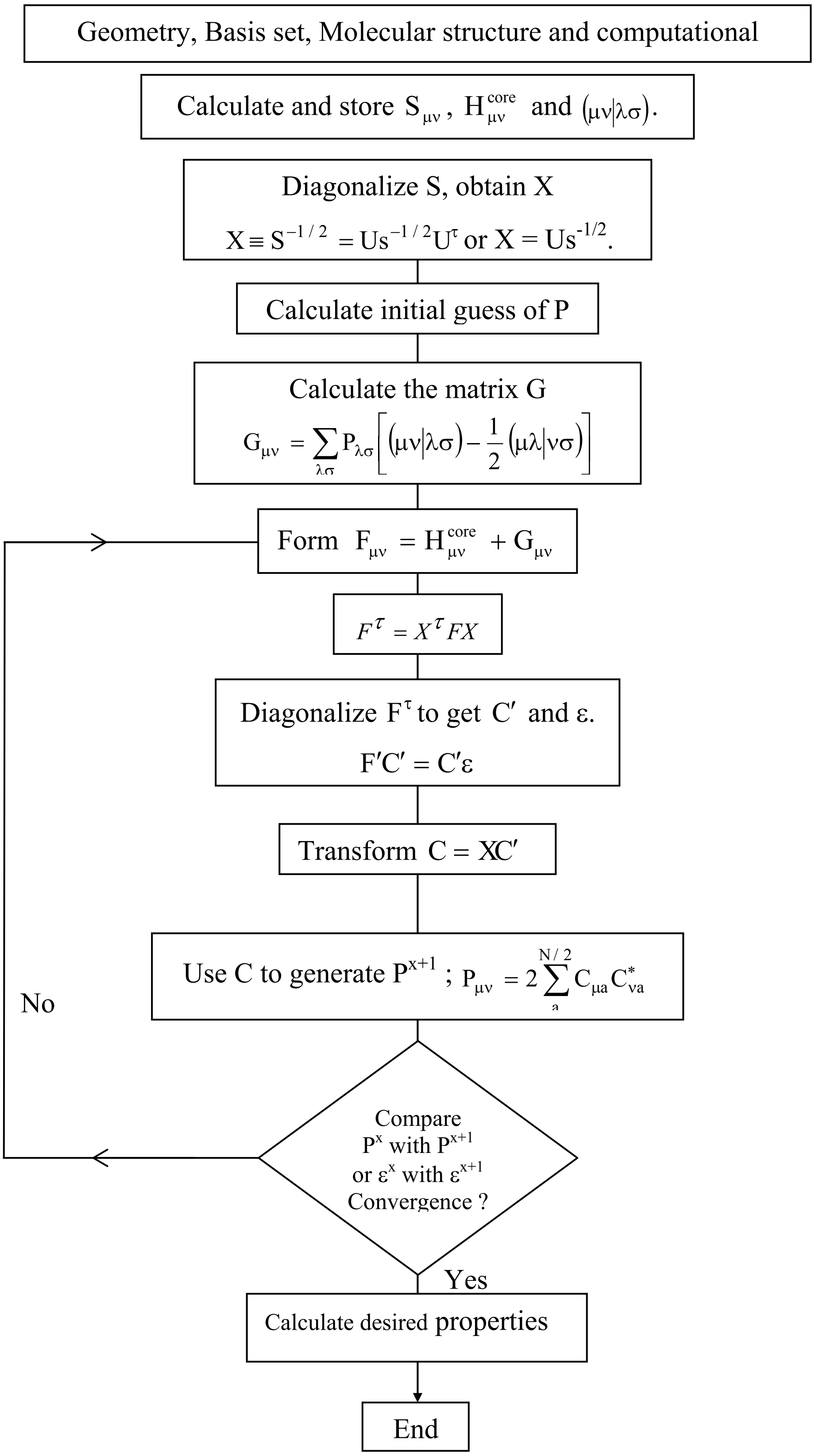

Figure A1 Schematic view of a Hartree-Fock self consistent field calculation.

Basis Set

The basis set most commonly used in quantum mechanical calculations are composed of atomic functions. The next approximation involves expressing the molecular orbitals as linear combinations of a pre-defined set of one-electron functions known as basis function. An individual molecular orbitals is defined as:

$$\phi_i = \sum_{\mu=1}^{N} c_{\mu i}\chi_{\mu} \tag{36}$$

where the coefficients $c_{\mu i}$ are known as molecular orbital expansion coefficients. The basis function $\chi_1 \ldots \chi_N$ are also chosen to be normalized. Gaussian-type atomic functions were used as basis functions. Gaussian functions have the general form

$$g(\alpha, \vec{r}) = cx^n y^m z^l e^{-\alpha r^2} \tag{37}$$

where $\vec{r}$ is of course composed of x, y, and z. α is a constant determining the size (radical extent) of the function. In Gaussian function, $e^{-\alpha r}$ is multiplied by powers (possibly 0) of x, y, and z and a constant for normalization, so that:

$$\int_{\text{allspace}} g^2 = 1 \tag{38}$$

Thus, c depends on α, l, m, and n.

Here are three representative Gaussian functional (s, p_y and d_{xy} types, respectively):

$$g_s(\alpha, \vec{r}) = \left(\frac{2\alpha}{\pi}\right)^{3/4} e^{-\alpha r^2}$$

$$g_y(\alpha, \vec{r}) = \left(\frac{128\alpha^5}{\pi^3} \right)^{1/4} y e^{-\alpha r^2}$$

$$g_{xy}(\alpha, \vec{r}) = \left(\frac{2048\alpha^7}{\pi^3} \right)^{1/4} xy e^{-\alpha r^2} \tag{39}$$

Linear combinations of primitive gaussians like these are used to form the actual basis functions; the latter are called contracted Gaussians and have the form

$$\chi_\mu = \sum_P d_{\mu p} g_p \tag{40}$$

where the $d_{\mu p}$'s are fixed constants within a given basis set. Note that contracted functions are also normalized in common practice. A few commonly used basis sets are lists as following.

Minimal Basis Sets: Minimal basis sets contain the minimum number of basis functions needed for each atom, as in these examples:

H: 1s
C: 1s, 2s, $2p_x$, $2p_y$, $2p_z$

Minimal basis sets use fixed-size atomic-type orbitals. The STO-3G basis set is a minimal basis set (although it is not the smallest possible basis set). It used three gaussian primitives per basis function, which accounts for the “3G” in its name. “STO” stands for “Slater-type orbitals,” and the STO-3G basis set approximates Slater orbitals with gaussian functions.

Split Valence Basis Sets

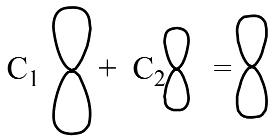

The first way that a basis set can be made larger is to increase the number of basis functions per atom. Split valence basis sets, such as 3-21G and 6-31G, have two (or more) sized of basis function for each valence orbital. For example, hydrogen and carbon are represented as:

H: 1s, 1s’
C: 1s, 2s, 2s’, $2p_x$, $2p_y$, $2p_z$, $2p'_x$, $2p'_y$, $2p'_z$

where the primed and unprimed otbitals differ in size.

The double zeta basis sets, such as the Dunning-Huzinaga basis set (D95), form all molecular orbitals from linear combinations of two sized of functions for each atomic orbital. Similarly, triple split valence basis sets, like 6-311G, use three sizes of contracted functions for each orbital-type.

Polarized Basis Sets

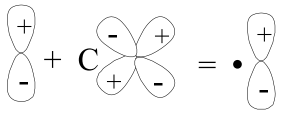

Split valence basis sets allow orbitals to change size, but not to change shape. Polarized basis sets remove this limitation by adding orbitals with angular momentum beyond what is required for the ground state to the description of each atom.
For example, polarized basis sets add d functions to carbon atoms and f functions to transition metals, and some of them add p functions to hydrogen atoms.

So far, the only polarized basis set 6-31G(d) is used. Its name indicates that it is the 6-31G basis set with d functions added to heavy atoms. This basis set is becoming very common for calculations involving up to medium-sized systems. This basis set is also known as 6-31G*. Another popular polarized basis set is 6-31G(d,p), also known as 6-31G**, which adds p functions to hydrogen atoms in addition to the d functions on heavy atoms.

Diffuse Functions

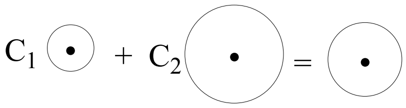

Diffuse functions are large-size versions of s- and p- type functions (as opposed to the standard valence-size functions) which allow orbitals to occupy a larger region of space. Basis sets with diffuse functions are important for systems where electrons are relatively far from the nucleus: molecules with lone pairs, anions and other systems with significant negative charge, systems in their excited states, systems with low ionization potentials, descriptions of absolute acidities. The 6-31+G(d) basis set is the 6-31G(d) basis set with diffuse functions added to heavy atoms. The double plus version, 6-31++G(d), adds diffuse functions to the hydrogen atoms as well. Diffuse functions on hydrogen atoms seldom make a significant difference in accuracy.

High Angular Momentum Basis Sets

Even larger basis sets are now practical for many systems. Such basis sets add multiple polarization functions per atom to triple zeta basis set. For example, the 6-31G(2d) basis set adds two d functions per heavy atom instead of just one, while the 6-311++G(3df,3pd) basis set contains three sets of valence region functions, diffuse functions on both heavy atoms and hydrogens, and multiple polarization funtions:3 d functions and 1 f function on heavy atoms and 3 p functions and 1 d function on hydrogen atoms. Such basis sets are useful for describing the interactions between electrons in electron correlation methods.

Semi-empirical Calculations

Because both time and storage requirements of an *ab initio* Hartree-Fock calculation increase as the fourth power of the number of basis functions, calculations on large molecules even with the smallest basis sets are apt to be prohibitive. In such situations, the NDDO (neglect of diatomic differential overlap) formalism affords practical methods for calculating the electronic structure of large systems. Here, only one- and two-centre, two-electron integrals are considered, and the Hartree-Fock matrix, consists only of elements for which basis functions μ and ν are on the same atom, and basis functions λ and σ are on another atom. The individual terms are defined below (the sum α is over all other atoms).

$$F_{\mu\mu} = H^{\text{core}}_{\mu\mu} + \sum_{\nu} P_{\nu\nu}\left[\langle \mu\mu \mid \nu\nu \rangle - \langle \mu\nu \mid \mu\nu \rangle\right] + \sum_{\delta}\sum_{\lambda}\sum_{\sigma} P_{\lambda\sigma}\langle \mu\mu \mid \nu\nu \rangle$$

$$F_{\mu\nu} = H^{\text{core}}_{\mu\nu} + P_{\mu\nu}\left[3\langle \mu\nu \mid \mu\nu \rangle - \langle \mu\mu \mid \nu\nu \rangle\right] + \sum_{\delta}\sum_{\lambda}\sum_{\sigma} P_{\lambda\sigma}\langle \mu\nu \mid \lambda\sigma \rangle$$

$$F_{\rho\lambda} = \beta_{\rho\lambda} - \frac{1}{2}\sum_{\nu}\sum_{\sigma} P_{\lambda\sigma}\langle \mu\nu \mid \lambda\sigma \rangle \qquad (41)$$

The elimination of three- and four-centre integrals greatly reduces the time and storage requirements for an NDDO calculation (which now increase as the square of the number of atoms) relative to that for a full Hartree-Fock treatment.

Three levels of NDDO theory are included in *SPARTAN'S SEMI EMPIRICAL* module:

MNDO Modified Neglect of Diatomic Overlap
AM1 Austin Method 1
PM3 MNDO Parameterization Method 3

In all of these formalisms, only the valence electrons are considered. The one-electron terms are given by,

$$H_{\mu\nu}^{core} = U_{\mu\nu} - Z_A \sum_{B \neq A} Z_B \langle \mu\nu | \delta\delta \rangle \qquad (42)$$

Here, μ and ν are located on atom A and the summation is over all other atoms. Uνν is related to the binding energy of an electron in atomic orbital ν, and is determined from spectroscopic data. Uνμ is set to zero for ν ≠ μ. The second term in equation 42 represents the attraction on an electron on atom A from the nuclear framework. The two center integral involves only the s function on atom B. Z_A is the charge of atom A without its valence electrons.

All one-centre, two-electron integrals (νν|μμ) and (νμ|νμ) are fitted to spectroscopic data. The two-centre, two-electron repulsion integrals (νμ|λσ) are approximated by classical multipole-multipole charge interactions between atoms A and B. The multipole charge separations within an atom are treated as adjustable parameters, i.e. optimized to fit the experimentally derived one-centre integrals.

The βμλ terms appearing in the Fock matrix (equation 41) are the one-electron, two-centre core resonance integrals and are approximated as,

$$\beta_{\rho\lambda} = \frac{\beta_\rho + \beta_\lambda}{2} S_{\rho\lambda} \qquad (43)$$

where $S_{\alpha\beta}$ is the overlap integral between Slater orbitals α and β, and $\alpha\beta$ and $\beta\alpha$ are adjustable parameters optimized using experimental thermo chemical data for simple molecules. Because all of the adjustable parameters are rooted in experimental data, these methods are known as semi-empirical. As in *ab initio* Hartree-Fock calculations, an SCF procedure is used to converge on a density matrix, and the electronic energy.

The three methods differ only in the core-repulsion terms (they also differ in the detailed parameterization). Core repulsion includes nuclear repulsion and non-valence electron-electron repulsion, which are not explicitly considered in the calculation of the electronic energy. In the MNDO model, the core repulsion energy is given by,

$$E^{CR} = \sum_{A \neq B} \sum_{B \neq A} Z_A Z_B \langle \delta(A) | \delta(B) \rangle \left(e^{-\sigma_a E_{AB}} + e^{-\sigma_B E_{AB}} \right) \qquad (44)$$

where Rαβ is the internuclear distance and αA and αB are adjustable parameters fit to give the correct empirical behavior. Details are provided in the original papers. MNDO tends to overestimate core repulsion between two atoms at van der Waals distances. For this reason, the AM1 model was developed.

In AM1 a sum of Gaussians is employed to better represent the core repulsion behaviour at van der Waals distances. PM3 uses a similar core repulsion function, but differs in the parameterisation procedure.

One advantage of methods parameterised using experimental data is their implicit inclusion of electron correlation effects. However, dependence on experimental data means that semi-empirical methods would not be expected to perform well on unusual types of molecules for which no data are available from which to construct parameters.

Density Functional Theory

Method s that are rooted in the so-called density functional theory are currently regarded as very promising since are able to include a large amount of correlation effects in a formalism that essentially requires very similar computational resources as the Hartree-Fock procedure. In fact the algorithms of the approach, in which the electron density is described in terms of one-electron basis functions, are very similar to the single-determinant HF algorithm. This property has helped to establish density functional methods as a standard tool for chemistry and physics.

While the concept of expressing part or all of the molecular energy as a functional of the electron density goes back to the early days of quantum theory, Density Functional Theory (DFT) was put on a rigorous theoretical foundation by the Hohenberg-Kohn theorem. It states that there exists unique density (ρ) that yield the exact ground energy of system. The subsequent work of Kohn and Sham laid the basis for practical computational applications of the DFT to real systems. The basis of their formalism is the so-called Kohn-Sham equations.

$$H\Psi_i = E_i\Psi_i \tag{45}$$

in which the Hamiltonian H is defined as

$$H = \left(-\frac{1}{2}\nabla^2 + V_{KS}\right) \tag{46}$$

where V_{KS} is a local potential defined such that the total density of the non-interacting system

$$\rho = \sum_i |\Psi_i|^2 \tag{47}$$

is the same as the density of the "real" system. V_{KS} has the three components V_{ext}, V_C and V_{XC} containing the nuclear and external, Coulomb potential of the electrons and the exchange-correlation interactions.

$$E_{KS} = V_{ext} + \sum_{\mu\nu} P_{\mu\nu}H_{\mu\nu} + \frac{1}{2}\sum_{\mu\nu\lambda\sigma} P_{\mu\nu}P_{\lambda\sigma}\Im + E_x(P) + E_C(P) \tag{48}$$

In most cases the expressions for E_C and E_X cannot be computed analytically and must be obtained by numerical methods. The key difference between the Hartree-Fock and Kohn-Sham approaches to the SCF methods is the term E_{XC}, which was mostly omitted in above discussion. In HF theory, this E_{XC} is written as

$$E_{XC}^{HF} = \frac{1}{2} \sum_{\mu\nu\lambda\sigma} (P_{\mu\nu}^{\alpha} P_{\lambda\sigma}^{\alpha} P_{\mu\nu}^{\beta} P_{\lambda\sigma}^{\beta})(\mu\nu / \lambda\sigma) \qquad (49)$$

while the KS theory introduces a functional

$$E_{XC}^{HF} = \int f(\rho^{\alpha}, \rho^{\beta}, \gamma_{\alpha\alpha}, \gamma_{\alpha\beta}, \gamma_{\beta\beta}) dr \qquad (50)$$

for the description. The density gradient invariants γ $(\gamma_{xy} = \nabla\rho_x \nabla\rho_y)$

Density Functionals

It is often customary to make a partition of the density functional into an exchange and correlation part for the separation of

$$E_{XC}(\rho) = E_X(\rho) + E_C(\rho) \qquad (51)$$

Although distinction between exchange and correlation contributions is somewhat artificial in the context of DFT, the above separation considerably simplifies the discussion. It should, however, be explicitly noted that the definition of E_C does not correspond to the *ab initio* EC since correlation has, by definition, meaning only in a mean field approximation and DFT is not using such an approximation. The exchange part, on the other hand, follows closely the HF definition of exchange, does however not necessarily reproduce the exact exchange.

Exchange

The exchange energy of a uniform spin-polarized gas of spin density ρ_σ is

$$E_X^S = -\sum \int \rho^\sigma(r) f_X^S(\rho_\sigma(r))dr \tag{52}$$

with $f_X^S(\rho_\sigma(r)) = \alpha_X[\rho_\sigma(r)]^{\frac{1}{3}}$ and $\alpha_X = \frac{3}{2}\left(\frac{3}{4\pi}\right)^{\frac{1}{3}}$. The exchange expression is sometimes lebeled *Slater exchange*, thus the superscript *S*. This exchange expression serves as a base for other functional, which can be conveniently expressed in terms of their enhancement factor F_X over the exchange of the uniform electron gas

$$E_X = -\sum_\sigma \int \rho_\sigma(r) f_X^S(\rho_\sigma(r)) F_X(\rho_\sigma), \gamma_{\sigma\sigma}(r))dr \tag{53}$$

For instance, the exchange functional proposed by Perdew and Wang uses the following factor:

$$F_X^{PW}(s) = \left[1 + 0.0864\frac{s^2}{m} + bs^4 + cs^6\right]^m \tag{54}$$

with $m = 1/15$, $b = 14$, $c = 0.2$ and $s = (24\pi^2)^{-1/3}\sqrt{(\gamma_{\sigma\sigma}/\rho^{4/3})}$ $\gamma_{\sigma\sigma}$ here is again the squared density gradient ∇_ω^2. One of the most used exchange functionals is that of Becke 1988, which is often labeled B88 or simply *B*.

$$F_x^B = 1 - \frac{\beta}{\alpha_x}, \frac{x^2}{1 + 6\beta \sinh^{-1}(x)} \tag{55}$$

which uses the values $x = \sqrt{(\gamma_{\sigma\sigma}/\rho_\sigma^{4/3})}$ and $\beta = 0.0042$ in order to maintain correct boundary conditions. In a different approach, Perdew and Wang proposed an exchange formula that is designed from purely first principles.

$$F_X^{PW91} = \frac{1+(a_1 s)(a_2 s)\sinh^{-1} + (a_3 + a_4 \exp(-100s^2))s^2}{1+(a_1 s)(a_2 s)\sinh^{-1} + a_5 s^4} \quad (56)$$

where $a_1 = 0.19645$, $a_2 = 7.7956$, $a_3 = 0.2743$, $a_4 = -0.1508$, $a_5 = 0.004$ and s the same as in eq. 32.

In practice, the three above exchange functionals are very similar, and are in fact based on minor corrections to the previous ones. Therefore they can be expected to produce very similar results. The enhancement over the simple electron gas, however, are significant enough and usually constitute constitute a major improvement.

Correlation

While it is possible to obtain E_C by some numerical methods from E_{XC} and the already known EX (cf. eq. 31) for the uniform electron gas, it is much more common to use separate correlation functionals. Distinction is made between local and gradient corrected functionals, referring to absence or presence of first order terms of the density ρ_σ. The local functional proposed by Vosko, Wilk and Nusair (VWN) was obtained using Pad'e approximated interpolations of Ceperley and Alder results of their accurate quantum Monte Carlo calculations for the homogeneous electron gas. The functional is,

$$E_C^{VWN} = \frac{A}{2}\left[\ln\frac{x^2}{X(x)} + \frac{2b}{Q}\tan^{-1}\frac{Q}{2x+b} - \frac{bx_0}{X(x_0)}\left(\ln\frac{(x-x_0)^2}{X(x)} + \frac{2(b+2x_0)}{Q}\tan^{-1}\frac{Q}{(2x+b)}\right)\right] \quad (57)$$

where the functions $x = r_b^{1/2}$, $X(x) = x^2 + bx + c$ and $Q = (4c - b^2)^{1/2}$ and the constants are $A = 0.0621814$, $x_0 = -0.409286$, $b = 13.0720$ and $c = 42.7189$. r_b represents are the Wigner-radius and is defined by $1/\rho = \frac{4\pi}{3}(r_b)^3$. Together with the exchange expression from eq. 40 this constitutes what is often called the local density approximation (LDA) or local spin density approximation (LSDA) when spin is considered (Gies and Gerhardts, 1987).

Due to the experiences with the LDA and as a consequence of some of its shortcomings, recent developments have resulted in a number of gradient corrections to local functionals like the aforementioned VWN or a completely new class of gradient corrected functionals.

Another frequently used functional has been published by Lee, Yang and Parr. It replaces both the local and the gradient part of the LDA correlation functional.

$$E_C^{LYP} = -a\frac{1}{1+d\rho^{-1/3}}\left\{\rho + b\rho^{-2/3}\left[C_F\rho^{-5/3} - 2t_w + \frac{1}{9}\left(t_w + \frac{1}{2}\nabla^2\rho\right)\right]e^{-2c\rho^{-1/3}}\right\} \quad (58)$$

where $t_w = \frac{1}{8}\left(\frac{|\nabla\rho|^2}{\rho} - \nabla^2\rho\right)$ and $C_F = \frac{3}{10}(3\pi^2)^{2/3}$, $a = 0.04918$, $b = 0.132$, $c = 0.2533$ and $d = 0.349$

Hybrid Functionals

More recently, following an approach proposed by Becke, the combination of DFT functionals with *ab initio* formulations led to a class of expressions which are essentially a mixture of both DFT and HF contributions with fitted coefficients for each contribution. The aim of this approach is to provide expressions that include the full exchange contribution and avoid side-effects arising from a complete replacement of the DFT exchange expression by the HF one. As an example, the B3LYP functional looks like this:

$$E_{XC}^{B3LYP} = a_{X0}E_X^S + (1-a_{X0})E_X^{HF} + a_{X1}\Delta E_X^B + E_C^{VWN} + a_C\Delta E_C^{LYP} \quad (59)$$

with $a_{X0} = 0.80$, $a_{X1} = 0.72$ and $a_C = 0.81$, which are values fitted for a selected set of molecules to reproduce the heat of formation. The term E_X^{HF} is calculated using the Kohn-Sham orbitals in the manner of the HF procedure by computing the exchange integrals $(\mu\nu / \nu\mu)$. The B3LYP functional often uses $\Delta E_C^{3LYP} = E_C^{LYP} - E_C^{VWN}$.

Time Dependent Density Functional Theory

Ground-state DFT is based on the papers by Hohenberg and Kohn, and by Kohn and Sham. The main result is that the density of a system is identical to the density of an associated noninteracting particle system moving in a local potential $v_s(r)$ defined by the Kohn-Sham equations (atomic units are used throughout):

$$\left[-\frac{1}{2}\nabla^2 + v_s[\rho(r)] \right] \varphi_i(r) = \varepsilon_i \varphi_i(r) \tag{60}$$

Here the local potential $v_s[\rho](r)$ is the so-called Kohn-Sham potential, consisting of the external potential v_{ext} (the Coulomb field of the nuclei and external fields if present), the Hartree potential v_H, which is trivially calculated from the density, and the *xc* potential v_{xc} which is the only unknown part:

$$v_s(r) = v_{ext}(r) + v_H(r) + v_{xc}(r) \tag{61}$$

The Kohn-Sham orbitals ϕ_i move in the effective field v_s which depends upon the electron density $\rho(r)$. This density is exactly obtained by summing the squares of the Kohn-Sham orbitals and multiplying by their occupation numbers *n_i*.

$$\rho(r) = \sum_i^{occ} n_i |\varphi_i(r)|^2 \tag{62}$$

As the KS potential $v_s(r)$ and the density $\rho(r)$ are inter-dependent, the equations have to be solved in a Self-Consistent Field (SCF) procedure, which means that one iteratively adapts the effective potential vs and the density ρ until the difference in the energy between two subsequent cycles is sufficiently small. In the most straightforward fashion, this can be performed by mixing the density of the previous cycle with a (small) part of the density in the present cycle. This "simple damping" approach usually converges very slowly, and in practice the Direct Inversion in the Iterative Subspace (DIIS) procedure by Pulay and co-workers, is much to be preferred. In the DIIS approach, not only the results of the previous cycle, but the results of all, or many, previous cycles are taken into account, in order to obtain the optimal guess for the next cycle. If one is close to self-consistency, this procedure converges quadratically. Using DIIS, it typically takes about five to fifteen cycles to convert the SCF equations above.

In order to solve the KS equations an approximation for the exchange-correlation (xc) potential $v_{xc}(r)$ is required and the simplest one is the LDA which is based upon the local density of the system. The GGAs go beyond this and take the local gradient of the density into account aswell, allowing for a much improved accuracy in the results for energies and geometries. Many other approximations, for examples those based directly on the KS orbitals, are also available.

The usual ground-state DFT scheme enables one to determine the density, and consequently the dipole moment, of a molecule with or without external electric fields (Gisbergen *et al.*, 1989, 1999). This affords the determination of the static polarizability and hyperpolarizability tensors α, β and γ, by performing calculations in small electric fields of varying magnitudes and directions. In this so-called finite field (FF) approach, the tensors are then determined from finite difference techniques. The main advantage of this approach is that no programming work is needed. Any standard DFT code will allow the determination of static properties in this Manner. However, for the determination of higher-order tensors, such as γ, one needs very well-converged solutions to the KS equations in order to make reliable predictions, which may be technically hard to achieve and which will certainly lead to considerable increases in CPU time.

The most fundamental disadvantage of the FF approach, however, is that one has access to static properties only. The frequency-dependent polarizability and hyperpolarizability tensors are not accessible. Excitation energies and oscillator strengths can also not be obtained from the FF calculations. This is an important drawback of the FF approach, as it makes a direct comparison with experimental results impossible. Especially for hyperpolarizabilities, it is known that there are substantial differences between the frequency-dependent and zero frequency results.

If one is interested in the time dependent properties mentioned above (Bartolotti, 1981, 1982), a time dependent theory is required. In the DFT framework, this means that one has to start from the time dependent KS (TDKS) equations as derived by Runge and Gross;

$$i\frac{\partial}{\partial t}\varphi_i(r,t) = \left[-\frac{\nabla^2}{2} + v_s(r,t)\right]\varphi_i(r,t) \equiv F_s\varphi_i(r,t) \qquad (63)$$

The time dependent KS potential $v_s(r,t)$ is subdivided in the same manner as its static counterpart:

$$v_s(r,t) = v_{ext}(r,t) + v_H(r,t) + v_{xc}(r,t) \qquad (64)$$

the Hartree potential being explicitly given by:

$$v_H(r,t) = \int dr' \frac{\rho(r',r)}{|r-r'|} \qquad (65)$$

and the time dependent *xc* potential $v_{xc}[\rho](r,t)$ being an unknown functional of the time dependent density $\rho(r,t)$ now given by:

$$\rho(r,t)=\sum_{i}^{occ} n_i \left|\varphi_i(r,t)\right|^2 \tag{66}$$

If a certain approximation for the time-dependent *xc* potential $v_{xc}(r,t)$ has been chosen, the TDKS equations can be solved iteratively to yield the time dependent density of a system, which may be exposed to an external time dependent electric field. If one is interested in the effects due to extremely large laser fields, the perturbative expansion of the dipole moment becomes meaningless, and the TDKS equations have to be solved non-perturbatively. This has until now been performed for atoms, by Ullrich and Gross (Hirata *et al.*, 1999), and more recently also by others, and gives access to such effects as higher harmonic generation (HHG), which are not accessible in a perturbative approach. The drawback of this is that the calculations are very time consuming, forbidding the treatment of medium-sized molecules. If one restricts oneself to properties which are accessible through perturbative methods, as we will do here, a much more efficient approach is possible, allowing the treatment of large molecules (>100 atoms). This approach will be the subject of the next section. For more information on time dependent DFT in general, the reader is referred to the excellent reviews by Gross and coworkers.

Appendix B: Publication

Theoretical Study The Structures and Electronic Properties of Oligo(para-Phenylene-Vinylene) Carboxylic Acid and Its Derivatives

Piriyagagoon, A., S. Suramitr and S. Hannongbua

The Proceeding of 34th Congress on Science and Technology of Thailand (STT 34), Queen Sirikit National Convention Center, Bangkok, Thailand, October 31 – November 2, 2008.

CURRICULUM VITAE

NAME : Mr. Apipol Piriyagagoon

BIRTH DATE : August 15, 1984

BIRTH PLACE : Ratchaburi, THAILAND

EDUCATION :

YEAR	**INSTITUTION**	**DEGREE/DIPLOMA**
2006	Kasetsart University	B.Sc. (Chemistry)

POSITION/TITLE : Postgraduetes student

WORKPLACE : Faculty of Science, Kasetsart University

SCHOLARSHIP : Development and Promotion of Science and Technology Talents Project (DPST)

PUBLICATION : Piryagagoon, A., S. Suramitr and S. Hannongbua, Theoretical Study The Structures and Electronic Properties of Oligo(para-Phenylene-Vinylene) Carboxylic Acid and Its Derivatives, The 34th Congress on Science and Technology of Thailand (STT 34), Queen Sirikit National Convention Center, Bangkok, Thailand, October 31 – November 2, 2008